CrossMark

Gas-phase formation during thermal energy storage in near-surface aquifers: experimental and modelling results

Klas Lüders[1] · Linda Firmbach[2] · Markus Ebert[1] · Andreas Dahmke[1] ·
Peter Dietrich[2] · Ralf Köber[1]

Abstract Heating of groundwater by thermal energy storage (TES) poses a potential for the formation of a separate gas phase. Necessary boundary conditions, potential effects and monitoring feasibility of this process were not focused within previous studies. Since the formation of a gas phase could change groundwater flow conditions, hydrochemistry, porous media properties and thus efficiency of TES applications, improved understanding of the process is needed. The temperature of percolated sediment column tests was adjusted to 10, 25, 40 and 70 °C to quantify temperature-induced physical gas-phase formation and its effect on electrical resistance. Gas-phase formation, its accumulation and effects on hydraulic conductivity, heat conductivity and heat capacity were investigated using scenario calculations based on a closed-loop borehole TES system at 60 °C for different geochemical conditions. Experimentally quantified degassing ratios were within the expected range of thermodynamic calculations. The laboratory time-lapse electrical resistivity measurements proofed as a suitable tool to identify the onset and location of the gas-phase formation. Depending on the geochemical conditions, hydraulic conductivity in the area of the simulated heat storage site decreased between 60% and up to one order of magnitude in consequence of degassing within the scenario calculations. Heat conductivity and heat capacity decreased by maximally 3 and 16%, respectively. The results indicate that gas-phase formation as a result of aquifer heating can have pronounced effects especially on groundwater flow conditions and therefore should be considered particularly for nearly or fully gas-saturated groundwater and aquifers containing gas sources.

Introduction

Changes in global energy supply towards more renewables are necessary to achieve worldwide objectives of climate protection (IEA 2015). Renewable energies reached 27.8% of the gross electricity consumption in Germany by 2014 and took over the role as most important power source from the brown coal (BMWi 2015). Beside the achievements in electricity generation, the share of renewable energies on heat production remained at around 10% since 2010 (BMWi 2015), although especially heating and acclimatisation hold capacious potentials to reduce CO_2 emissions (IEA 2015). Improvements in efficiency as e.g. storing surplus heat from solar thermal applications or industrial processes in shallow aquifers are a feasible possibility to enhance the share of renewable energies on heat supply (Schmidt and Müller-Steinhagen 2005). In addition, Bauer et al. (2015) suggest not only to use surplus heat but to convert surplus energy from other renewable

This article is part of a Topical Collection in Environmental Earth Sciences on ''Subsurface Energy Storage'', guest edited by Sebastian Bauer, Andreas Dahmke, and Olaf Kolditz.

✉ Klas Lüders
  khebbeln@gpi.uni-kiel.de

[1] Institute of Geosciences, Kiel University, Kiel, Germany

[2] Helmholtz Centre for Environmental Research – UFZ, Leipzig, Germany

power generation technologies as e.g. wind energy into heat for seasonal heat storage in the subsurface. For underground thermal energy storage (UTES) applications, Schmidt and Müller-Steinhagen (2005) reported maximum temperatures of ~ 90 °C. Near-surface aquifers can also be used for cyclic storage of heat and cold for heating and climatisation of houses or commercial buildings in winter and summer times (Bridger and Allen 2005).

Besides these potential economic advantages, the installation and operation of geothermal plants using near-surface aquifers for heat storage may affect hydrological and hydro-geochemical properties of the underground. Since there is no monitoring obligatory, only some single-point measurements at greater plants have been carried out but are rarely published. For example, Possemiers et al. (2014) analysed the temperature changes induced by seven aquifer thermal energy storages (ATES). Their results indicate no immediate risk for groundwater quality. On the other hand, Bockelmann et al. (2012) found at a geothermal system with 36 borehole heat exchangers (BHS) an inefficient operation indicated by more heat injection in summer time than extraction in winter. This results in a warming of the underground to such a high level that the plants cooling mode is impaired. Given the lack of time and cost-efficient spatial high-resolution monitoring methods and the "unfinished business" in national and international regulations (Ferguson 2009; Hähnlein et al. 2010; Bonte et al. 2011) concerns arise about possible negative long-term impacts for groundwater and soil.

Temperature changes in the shallow subsurface induced by underground thermal energy storage (UTES) may alter groundwater geochemistry through reactions triggered by the temperature dependence in the solubility of minerals and gases, sorption and ion exchange equilibria or kinetic rate constants. Previous studies mainly focused on sediment–water interactions (Willemsen and Appelo 1985; Holm et al. 1987; Brons et al. 1991; Griffioen and Appelo 1993; Arning et al. 2006; Bonte et al. 2013a, b; Jesußek

et al. 2013; Possemiers et al. 2014; Saito et al. 2016) while the formation of a separate gas phase which gets favoured by the decreasing gas solubilities with induced temperature increases was addressed only marginally. Jenne et al. (1992) suggested to keep up an overpressure in aquifers with high dissolved gas concentrations to avoid the formation of a separated gas phase. Bonte (2013) proposed the observation of partial gas pressures within aquifers in running heat storage applications to monitor the possibility of a gas-phase formation. None of the studies investigated the specific physical and geochemical aquifer preconditions favouring or preventing the formation of a separate gas phase. The initial dissolved gas concentrations with respect to the corresponding solubility are key factors to assess the probability of a gas-phase formation. Unfortunately, except oxygen and carbon dioxide, dissolved gas concentrations are not measured as a matter of routine. O_2 concentrations tend to be lower in near-surface aquifers than in equilibrium with the atmosphere as O_2 concentrations decrease by oxygen consumption in the vadose zone and the aquifer in case organic material and/or reduced substances as e.g. metal sulphides are available (e.g. Appelo and Postma 2005). In contrast, N_2 concentrations will rather increase due to nitrate reduction (e.g. Appelo and Postma 2005) leading to higher dissolved concentrations of N_2 compared to equilibrium with the atmosphere as indicated by the dissolved gas pressures observed in several studies addressing groundwater dating or effects of land use on groundwater chemistry (see Table 1).

Dissolved gas concentrations of CO_2, H_2S and CH_4 can also be increased by organic matter or organic pollutant degradation (e.g. Appelo and Postma 2005). The contribution to dissolved gas concentrations by organic carbon degradation is controlled by the availability of degradable organic carbon, the degradation rate and degradation pathway. An induced temperature increase can have an impact on all three of these aspects: enhanced dissolved organic carbon mobilisation due to increased temperatures

Table 1 Statistical distribution of occurring dissolved gas pressures

Percentile	N_2 ($n = 82$) [atm]	O_2 ($n = 40$) [atm]	CO_2 ($n = 10$) [atm]	Ar ($n = 82$) [atm]	$\sum$ ($n = 82$) [atm]
0th (minimum)	0.54	0.000	0.0046	0.00014	0.55
5th	0.65	0.000	0.0046	0.00017	0.65
25th	0.77	0.000	0.0097	0.00857	0.85
50th (median)	0.98	0.010	0.0108	0.00932	1.02
75th	1.14	0.105	0.0117	0.01017	1.17
95th	1.40	0.131	0.0146	0.01124	1.41
100th (maximum)	1.58	0.190	0.0193	0.01622	1.59

Raw data were taken from Vogel et al. (1981), Wilson et al. (1990), Feast et al. (1998), Tesoriero et al. (2000), Puckett and Cowdery (2002), Andrews et al. (2005), Visser et al. (2007, 2014) and Alikhani et al. (2016)

has been measured in column experiments at 60 °C (Bonte et al. 2013b), in batch experiments with a peaty clay and a quartz-rich sand at temperatures above 45 °C (Brons et al. 1991) and in batch experiments with a lignite sand at 70 °C (Jesußek et al. 2013). Bonte et al. (2013a) and Jesußek et al. (2013) observed a temperature-induced shift in organic carbon degradation towards more reducing pathways. While the reduction rate of nitrate increased steadily with temperature (Jesußek et al. 2013), the sulphate reduction rate increased up to 45 °C, showed a distinct minima at the mesophilic–thermophilic transition around 50 °C and increased again from 50 up to 70 °C (Bonte et al. 2013a).

At ambient groundwater temperatures, the formation of a separate gas phase can be caused by denitrification processes in a riparian wetland (Blicher-Mathiesen et al. 1998) or by methanogenic degradation of petroleum hydrocarbons (Amos et al. 2005). Another possible source for high dissolved gas concentrations in shallow aquifers is the natural upward migration of gas from deeper layers as it has been observed for CO_2 (e.g. Battani et al. 2010) and CH_4 (e.g. Coldewey and Melchers 2011; McIntosh et al. 2014). Beside a natural upward migration, also leaky production wells have been reported to act as migration pathways for methane (e.g. Van Stempvoort et al. 2005). Temperature and pressure conditions in an aquifer control the solubility and thus also the saturation of any dissolved gases. The formation of a separate gas phase is therefore dependent on the site-specific interplay between initial dissolved gas concentrations, planned temperature increase and depth of the target aquifer.

Under field conditions, the spatially continuous observation of temperature variations with possible gas-phase formation as consequence caused by TES poses a challenge. Electrical resistivity (ER) monitoring can provide images of bulk ER variations which potentially could serve as proxy for assessing temperature variations and gas-phase formation. However, the imaged resistivity ground variability must be interpreted with regard to the requested target parameters, since the ER of the ground depends on various soil parameters, e.g. porosity, water content, temperature, grain size and shape, the particle orientation and cementation, mineral composition and ionic strength (Archie 1942; Dachnov 1962; Llera et al. 1990; Mualem and Friedman 1991; Friedman and Seaton 1998; Rhoades et al. 1999; Robinson and Friedman 2003; Corwin and Lesch 2005; Friedman 2005; Knödel et al. 2005; Brunet et al. 2010; McCleskey et al. 2011). Interpretation of a measured ER value with regard to changes in a distinct underlying parameter, e.g. temperature or water content, is usually not possible. However, using time-lapse measurements allows for monitoring the change in ER, which agrees for better inference of target parameter changes

from initial conditions. For example, Daily et al. (1992) and Hoffmann and Dietrich (2004) successfully employed time-lapse ER measurements for monitoring water flow in the ground, whereas Dietrich (1999) analysed ER to monitor salt tracer experiments. Gunn et al. (2014) monitored soil moisture in clay embankments using ER supporting preventative geotechnical asset maintenance, and Grellier et al. (2005) used time-lapse ER measurements for monitoring moisture changes in a bioreactor. ER measurements have been previously used in geothermal reservoir characterisation and monitoring of heat plumes. At laboratory scale, Giordano et al. (2013) evaluated surface ER measurements for monitoring groundwater and soil changes under induced temperature variations, whereas Hermans et al. (2012) used surface time-lapse ER measurements for monitoring the induced heat diffusion in a shallow geothermal field experiment. In a further step, Giordano et al. (2015) tested surface time-lapse ER measurements in their integrated approach from laboratory to field scale for an economic and ecological design and monitoring of ground TES. In another heat tracer experiment, Hermans et al. (2015) used cross-borehole time-lapse ER monitoring for quantifying induced temperature changes in the aquifer. However, the potential of ER measurements goes beyond monitoring heat flow in geothermal reservoirs, since the ER of porous sediments increases with growing fractions of gas phase in the pore fluid. This effect has already been used for different studies. Yang et al. (2015) used 3D cross-hole ER tomography monitoring a CO_2 migration in a shallow aquifer, while Bergmann et al. (2012) used surface-downhole ER tomography monitoring CO_2 storage in a sandstone 650 m below surface and Carrigan et al. (2013) used this method already for the monitoring of CO_2 in a deep geologic reservoir exceeding 3000 m below surface. Consequently, time-lapse ER should also be considered as potential monitoring method of possible gas-phase formation induced by geothermal energy storage.

The formation of a separate gas phase reduces hydraulic conductivity by lowering pore space water saturation in the zone of gas-phase formation. Insertion of oxygen in formerly water-saturated sand columns caused gas-phase saturations of 14–55% and a corresponding decrease in hydraulic conductivity of 38–95% (Fry et al. 1997). Degradation of ethanol by denitrification led to a gas-phase saturation of 23% in laboratory flow cell experiments conducted with an upward water flow whereupon the gas phase was assumed to mainly consist of N_2 (Istok et al. 2007). Formation of a CH_4 (20–85%), N_2 and CO_2 (15–80%) gas phase by methanogenic degradation of methanol lowered the hydraulic conductivity in sand columns by 75–97% under upward flow conditions (Sanchez de Lozada et al. 1994). Methanogenic degradation of

methanol caused formation of an unspecified gas phase which led to gas-phase saturations of 40–50% in the bioactive zone of gas-phase formation and up to 80% below the sealing in a sand-filled cell under lateral flow conditions (Ye et al. 2009). Correspondingly, Ye et al. (2009) calculated a decrease in hydraulic conductivity by 80–90% in the bioactive zone of gas-phase formation and by over 99% below the sealing. In contrast to such water saturation decreases due to gas-phase formation, the net effects of carbonate precipitation and silica dissolution at temperatures between 2 and 50 °C, with a maximum decrease in pore space of 0.2% calculated by Arning et al. (2006), appear to be of minor relevance. Instead, Palmer and Cherry (1984) expect the threat of clogging caused by temperature-induced carbonate precipitation in ATES systems primarily either within the pipe system or, in case precipitates forming within the pipes of the heating system remain in suspension, at the interface between well and aquifer. Beside changes in hydraulic conductivity, replacement of water by a gas phase affects further important parameters regarding efficiency of heat storage applications as e.g. heat conductivity and heat capacity.

Approaches to model a gas-phase formation by methanogenesis in a petroleum hydrocarbon contaminated aquifer have been undertaken by Amos and Mayer (2006) who included gas bubble formation and collapse depending on dissolved gas pressures into the reactive transport code MIN3P. Feedback on groundwater flow was considered, but the implementation did not allow any migration of gas bubbles. With these boundary conditions, methanogenic degradation of petroleum hydrocarbons on the field scale leads to induced residual source zone gas-phase saturations of more than 30% which resulted in a decrease in hydraulic conductivity to <25% (Amos and Mayer 2006). Krol et al. (2011) modelled gas bubble formation and mobilisation during subsurface heating of contaminated zones to 70, 80 and 90 °C. Gas-phase saturations increased up to a maximum of 30% in the source zone. In contrast to the Amos and Mayers (2006) approach, gas migration was included in the combined ETM-MIP model approach by Krol et al. (2011), but no feedback on groundwater flow was implemented.

None of the studies investigated gas-phase saturations with solely temperature-induced physical gas-phase formation under natural groundwater condition. Nevertheless, it was shown that a significant effect on aquifer hydraulics can be expected if a separate gas phase forms and accumulates over time. And since now, no gas-phase formation monitoring in geothermal reservoirs by means of time-lapse ER measurements has been carried out striving to monitor alteration of the natural conditions in the ground caused by geothermal installations. Therefore, in this study we focus on the following objectives:

- Do thermodynamic calculations on a gas-phase formation coincide with experimental results and are therefore a suitable tool to estimate a gas-phase formation in aquifers?
- Is it possible to monitor gas-phase formation and farther distribution of a gas phase in column tests using time-lapse ER measurements?
- Which extent of gas-phase formation with regard to different gases and different geochemical boundary conditions can be expected due to heat storage in near-surface aquifers?
- What hydraulic and thermic effects relating to efficiency of a heat storage site are caused by a gas-phase formation?

To assess these objectives, a combined approach using geochemical and geoelectrical measurements in laboratory column tests and proceeding hydrochemical scenario calculations is applied as described in detail in the following section.

Materials and methods

Column experiments

The column experiments within this study were predominantly designed to investigate temperature-induced changes in geochemical sediment–water interactions [in a similar set-up as it was used by Jesußek et al. (2013)]. The corresponding results will be published elsewhere. For the present study, the columns were additionally equipped with a gas trapping system to quantify the gas-phase formation. This quantification was done by building the ratio of forming gas phase in litre or millilitre of gas per litre of flowed through water to enable the transfer to further boundary conditions regarding groundwater flow speed. In addition, measurements of the gas-phase accumulation within the columns were performed. For the column experiments that were conducted at 10, 25, 40 and 70 °C, two Pleistocene sands differing mainly in grain size and organic carbon content (Table 2) from aquifers in Bönebüttel (sediment sample BS-Bönebüttel shallow) and Odderade (sediment sample OR; Table 2), Schleswig–Holstein, northern Germany, were used. The utilised HDPE columns were 110 cm long (internal diameter: 10 cm) and had nine sampling ports along the flow path with the distance in between increasing from the bottom to the top of the columns (Fig. 1). In order to avoid effects of variations in sediment composition with depth, eight (BS) and five (OR) metres of drilling cores were homogenised before filling the columns (Table 2).

The columns filled with sediment BS were operated using water from the same aquifer, whereas the ones

Table 2 Characteristics of the sediments used

	BS	OR
Sediment	Pleistocene sand	Pleistocene sand
Grain size	Slightly gravelly sand	Muddy sand
Depth	4–12 (m under ground level)	66–68, 69–72 (m under ground level)
Σ(Na, K, Ca, Mg, Fe, Mn)	1070 [mmol/kg]	1168 [mmol/kg]
$C_{org.}^a$	142 [mg/kg]	1830 [mg/kg]
$C_{carb.}^a$	5711 [mg/kg]	2322 [mg/kg]
Pyrite[a]	221 [mg/kg]	1208 [mg/kg]
Water in use	BS site water	Tap water

[a] Dethlefsen (2015, unpublished data)

containing OR sediment were percolated with tap water which had a composition comparable to the water in the corresponding aquifer. Four BS and four OR columns were filled alternately with water and sediment. To reach a homogeneous one-dimensional flow through the columns, the lower most 10 cm were filled with coarse-grained commercial quartz (1.0–2.5 mm) instead of sediment. The sediment was repeatedly consolidated while filling the columns to prevent gas-phase entrapment. The experimental set-up is shown in Fig. 1.

The groundwater serving as inflow solution (Table 3) was stored at 10 °C in gas-tight bags (PETP/AL/PE, tecotainer-inset; Tesseraux). A peristaltic pump (Ismatec Ecoline VC-MS/CA 8-6; Idex) pumped the inflow solution with 1 ml/min into the columns generating a flow from the

bottom upwards through the columns. The (pumping-) tubes (internal diameter 1 mm, wall thickness 1 mm) connecting the water storage bags with the columns were coated with aluminium foil to minimise gas diffusion into the solution. The outflow of the columns was connected to a water-filled gas trapping bottle on a scale which was heated to the same temperature as the corresponding column. Gas-phase formation ratios were measured by the decreasing weight of these gas trapping bottles as the water inside was replaced by gas bubbles flushed out of the columns from time to time.

All columns were equilibrated by percolation with the corresponding inflow solutions at 10 °C (±1 °C) for two (BS) and four (OR) months in a fridge before heating was started. One column per sediment remained in the fridge at
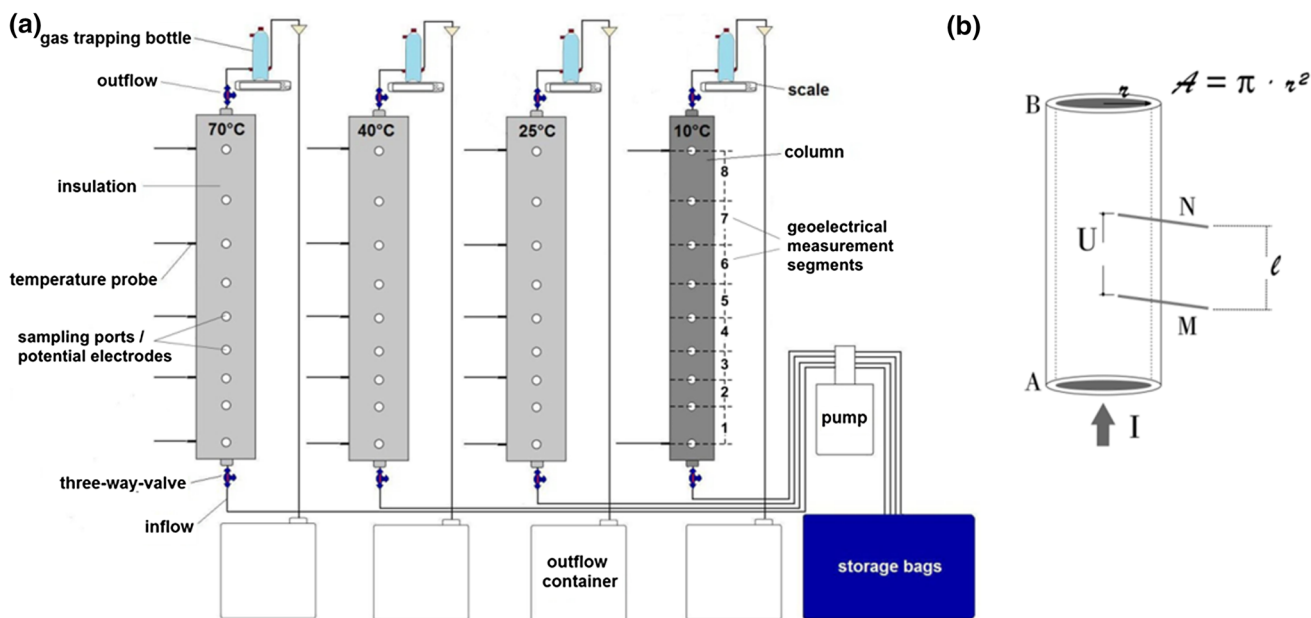

Fig. 1 Experimental column set-up to measure the trapped gas volume, ratio of degassing and electrical resistivities (**a**) whereupon an induced current I flows between the two current electrodes A and B while the potential difference U is measured between the adjacent potential electrodes M and N (**b**). Using the cross section A and the distance l between the potential electrodes the measured voltages can then be converted into the bulk resistivities of the respective volumes (**b**)

Table 3 Composition of inflow solutions for the OR and BS column experiments

		OR	BS
pH	[–]	7.69 ± 0.26	7.21 ± 0.15
TIC	[mmol/L]	5.91 ± 0.17	5.51 ± 0.11
NPOC	[mmol/L]	0.23 ± 0.08	0.40 ± 0.03
K^+	[mmol/L]	0.08 ± 0.01	0.05 ± 0.03
Na^+	[mmol/L]	0.64 ± 0.02	0.71 ± 0.03
Ca^{2+}	[mmol/L]	3.16 ± 0.05	3.41 ± 0.07
Mg^{2+}	[mmol/L]	0.36 ± 0.01	0.23 ± 0.01
Fe_{diss}	[mmol/L]	0.0001 ± 0.0002	0.0011 ± 0.0023
Mn_{diss}	[mmol/L]	0.0002 ± 0.0003	0.0031 ± 0.0007
Si_{diss}	[mmol/L]	0.50 ± 0.01	0.46 ± 0.01
Al_{diss}	[mmol/L]	0.0001 ± 0.00007	0.00012 ± 0.00005
Cl^-	[mmol/L]	0.87 ± 0.02	0.80 ± 0.04
NO_3^-	[mmol/L]	0.01 ± 0.01	0.001 ± 0.002
SO_4^{2-}	[mmol/L]	0.51 ± 0.02	0.92 ± 0.02
N_2	[mmol/L] ([atm])	0.51 ± 0.02 (0.60)	0.9 ± 0.04 (1.1)
O_2	[mmol/L] ([atm])	0.16 ± 0.05 (0.093)	0.01 ± 0.007 (0.0058)
CO_2	[mmol/L] ([atm])	0.29 ± 0.01 (0.0054)	0.75 ± 0.01 (0.014)
Σ dissolved gases	[mmol/L] ([atm])	0.96 ± 0.08 (0.70)	1.66 ± 0.05 (1.1)

10 °C as reference, while the other three columns were heated to 25 (±1), 40 (±2) and 70 °C (±2 °C) using heating tapes. Additionally, the heated columns were covered with a 1.9-cm-thick insulating mat (AF-19MM/E; Armacell). Temperature monitoring by Pt100 probes (for positions see Fig. 1) showed that heating up of the inflowing water to the aimed temperature was restricted to the gravel layer at the bottom of the columns. The volume of gas phase trapped within the sediment was additionally calculated for the BS column experiments using pressure changes induced by water injections (using the inflow solution) into closed columns following the law of Boyle–Mariotte (Eq. 1). Therefore, the pressure before water injection (p_1) divided by the pressure after water injection (p_2) was equalised to the volume after water injection (V_2) divided by the volume before water injection (V_1).

$$\frac{p_1}{p_2} = \frac{V_2}{V_1} \tag{1}$$

Water samples were retrieved from three-way valves at the in- and outflow of the columns as well as from the sampling ports along the flow path (Fig. 1) and geochemically analysed using standard methods. The results are not included in this study but will be presented elsewhere. Dissolved CH_4 and N_2 concentrations were measured using gas chromatographs (GC 6890plus, HS7694 (for CH4) and GC 7890B, HS 7697A (for N_2); Agilent). Liquid N_2 samples were taken directly from the gas-tight bags which contained the inflow solution and injected into closed, argon-flushed GC vials by using a gas-tight syringe to avoid contamination by air. Though, the lowest measured value of tenfold measurements was considered to be most accurate as all contamination by air would have increased the N_2 concentration. Oxygen was measured with a phase fluorimeter (Neofox-GT; Ocean Optics) and an oxygen sensor (FOSPOR-R-Series Sensor Probe; Ocean Optics) within a tube attached to the three-way valves where water diverged from the inflow, outflow or the sampling ports was flowing through.

Geoelectrical monitoring of gas-phase accumulation and distribution within the experimental columns

The measured electrical bulk resistivity is an integral value of the resistivity of the sediment matrix and the fluid in the pore space. The ER of sand grains significantly exceeds that of water filling the pore space. The electrical conductivity in the column is thus dominated by the electrolytic conductivity of the pore fluid, and hence, the measured bulk resistivity is governed by the resistivity of the pore water. Generally, the resistivity decreases with increasing temperature. Corwin and Lesch (2005) report a resistivity change of 1.9% per K, whereas Hem (1985) give 2% and Keller and Frischknecht (1966) report 2.5% per K.

Many authors describe the temperature dependence of the ER by referencing it to a known resistivity $\rho(T_{ref})$, at a special temperature

$$\rho(T) = f_T \cdot \rho(T_{ref}) \tag{2}$$

with f_T being a temperature-dependent conversion factor given differently by different authors (for a comprehensive review see Ma et al. (2011). Typical conversion values are given in Richards (1954). Dachnov (1962) formulated the relation for the reference value set to 18 °C with

$$\rho(T) = \frac{\rho(18\,°C)}{1 + \alpha_T(T - 18\,°C)} \tag{3}$$

where α_T is a temperature coefficient that decreases with increasing temperature. Around 18 °C, it is set to approximately 0.025. Using this equation, an expression not referring to a specific reference value can be derived:

$$\rho(T_2) = \rho(T_1) \frac{1 + \alpha_T(T_1 - 18)}{1 + \alpha_T(T_2 - 18)} \tag{4}$$

Thus, the reference conditions can be set arbitrary and the possibility of the comparison to another measured value can be done.

For sediments with negligible conductivity proportion of the matrix, Archie (1942) empirically found the following link between fluid resistivity ρ_f and bulk resistivity ρ_{sat} of fully water-saturated sediments

$$\rho_{sat} = F \cdot \rho_f \tag{5}$$

where F is the formation factor describing the geometry of the pore space. If the pore space is partially filled by a non-conductive gaseous phase, this affects the bulk resistivity similarly like a reduced porosity and Eq. 5 becomes

$$\rho_s = \frac{1}{S_w^n} \cdot \rho_{sat} \tag{6}$$

with ρ_s as the resistivity of sediments with water and gas phase in the pore space. S_w describes the degree of water saturation ($S_w = 1$ for full saturation) and n is the saturation exponent, a constant depending on soil properties, that is set to $n = 2$ for clean, consolidated or unconsolidated, water-wet sandstones (Archie 1942).

Many authors have investigated the effect of water saturation in the pore space on the electrical bulk resistivity of sediments. Keller and Frischknecht (1966) found a log-linear relation of saturation and resistivity for $S_w > 0.2$.

The geophysical measurements were done only for the second set of columns experiment (sediment BS). In ER applications, generally, four electrodes are used to measure the ground bulk resistivity. Two electrodes (A, B) are galvanically coupled to the ground material to inject a direct or very low-frequency alternating current signal of strength I (Fig. 1). The potential difference U (voltage) between another pair of electrodes (M, N) is recorded. The recorded voltage is a function of electrode arrangement and current strength (Knödel et al. 2005). In the column

experiments, the two current electrodes (A and B) were placed inside the column and fixed directly on the upper and lower HDPE cover of the cylindrical column (cf. Fig. 1). Both electrodes with the shape of circular discs of 10 cm diameter consisted of stainless steel and were installed prior to filling the column. The nine cannulas used for the groundwater sampling along the flow path served as potential electrodes (example in Fig. 1). Potential differences were recorded between adjacent cannulas (M, N) resulting in eight voltage measurements distributed along the vertical axes of the column as shown in Fig. 1. Measured voltages were converted into electrical resistance R by

$$R = \frac{U}{I} \tag{7}$$

and can be related to bulk resistivity ρ of the filled material by

$$\rho = R \cdot \frac{A}{l} \tag{8}$$

where l is the distance between the pair of voltage electrodes (M, N) and A is the inner circular area of the column (comparable to Fig. 1). However, based on the arrangement of the nine cannulas, the most upper and lowest segments of the columns could not be observed by the ER measurements (Fig. 1).

Measurements were carried out using a Resecs (RES6P, GeoServe) ER measurement device. Voltage measurements were repeated every 6 h over a period of 8 months. One measurement cycle resulted in eight voltage readings (cf. Fig. 1), which is one for every pair of electrodes and took approximately 2 min. During the first 2 months of recording, no heating took place to ensure a full adaptation of the columns to the constant surrounding temperature of 10 °C and to generate base measurements. Recorded data were stored automatically and regularly controlled by a human supervisor. Based on the quality of the checked data, the electrode coupling and system functionality was visually inspected and maintained if necessary.

Geochemical equilibrium modelling

Geochemical equilibrium modelling was done using the program PhreeqC v3.15 (Parkhurst and Appelo 2013) with the database PhreeqC.dat (argon data were obtained from the database llnl.dat also provided with PhreeqC v.3.15). In a first step, the measured ratio of gas-phase formation per litre water for the different temperatures was compared to the calculated ratio of gas-phase formation per litre water. For this purpose, the compositions of the inflow solutions and the experimentally investigated temperatures were set as input parameters (Table 4). The total pressure was set to

Table 4 List of initial 10 °C solutions used for the geochemical equilibrium and scenario calculations

Initial solution for	Background	pH [–]	N_2 [mmol/L]	H_2 [mmol/L]	O_2 [mmol/L]	CH_4 [mmol/L]	CO_2 [mmol/L]	H_2S [mmol/L]	Ar [mmol/L]	Results shown in
OR columns calculated	OR inflow (Table 3)	7.69	0.5	–	0.156	–	0.29	–	–	Figures 4a/5
BS columns calculated	BS inflow (Table 3)	7.21	0.857	–	–	–	0.75	–	–	Figures 4b/5
Equil. atmosphere	BS inflow (Table 3)	8.71	0.663	–	0.358	–	0.02	–	0.017	Figure 9a
Equil. to atm. w. incr. CO_2	BS inflow (Table 3)	6.65	0.663	–	0.273	–	2.70	–	0.017	Figure 9b
1–10 atm C(sat) N_2	Pure water	7	0.851–8.47	–	–	–	–	–	–	Figure 10a
1–10 atm C(sat) H_2	Pure water	7	–	0.881–8.83	–	–	–	–	–	Figure 10a
1–10 atm C(sat) O_2	Pure water	7	–	–	1.71–17	–	–	–	–	Figure 10a
1–10 atm C(sat) CH_4	Pure water	6.99	–	–	–	1.96–19.2	–	–	–	Figure 10a
1–10 atm C(sat) CO_2	Pure water	3.38–3.87	–	–	–	–	53.7–506	–	–	Figure 10a
1–10 atm C(sat) H_2S	Pure water	3.54–4.02	–	–	–	–	–	135–1237	–	Figure 10a
C(sat) N_2 in 30 steps	Pure water	7	0.0567–1.69	–	–	–	–	–	–	Figure 10b
C(sat) H_2 in 30 steps	Pure water	7	–	0.0588–1.75	–	–	–	–	–	Figure 10b
C(sat) O_2 in 30 steps	Pure water	7	–	–	0.114–3.4	–	–	–	–	Figure 10b
C(sat) CH_4 in 30 steps	Pure water	6.99–7	–	–	–	0.131–3.89	–	–	–	Figure 10b
C(sat) CO_2 in 30 steps	Pure water	3.72–4.46	–	–	–	–	3.53–106	–	–	Figure 10b
C(sat) CO_2 buff. in 30 steps	Calcite-buffered water	5.84–6.78	–	–	–	–	12.1–137	–	–	Figure 10b
C(sat) H_2S in 30 steps	Pure water	3.87–4.61	–	–	–	–	–	8.9–265	–	Figure 10b
Scenario A 0–10 m	BS inflow (Table 3)	7.21	0.849	–	0.005	–	0.74	–	–	Figures 11/12/16
Scenario B 10–11 m	BS inflow (Table 3)	7.21	0.849	–	–	2.06	0.74	–	–	Figures 13/14/16
Scenario B 11–12 m	BS inflow (Table 3)	7.21	0.849	–	–	2.25	0.74	–	–	Figures 13/14/16
Scenario B 12–13 m	BS inflow (Table 3)	7.21	0.849	–	–	2.45	0.74	–	–	Figures 13/14/16
Scenario B 13–14 m	BS inflow (Table 3)	7.21	0.849	–	–	2.64	0.74	–	–	Figures 13/14/16
Scenario B 14–15 m	BS inflow (Table 3)	7.21	0.849	–	–	2.84	0.74	–	–	Figures 13/14/16
Scenario B 15–16 m	BS inflow (Table 3)	7.21	0.849	–	–	3.03	0.74	–	–	Figures 13/14/16
Scenario B 16–17 m	BS inflow (Table 3)	7.21	0.849	–	–	3.23	0.74	–	–	Figures 13/14/16
Scenario B 17–18 m	BS inflow (Table 3)	7.21	0.849	–	–	3.42	0.74	–	–	Figures 13/14/16
Scenario B 18–19 m	BS inflow (Table 3)	7.21	0.849	–	–	3.62	0.74	–	–	Figures 13/14/16
Scenario B 19–20 m	BS inflow (Table 3)	7.21	0.849	–	–	3.81	0.74	–	–	Figures 13/14/16

Table 4 continued

Initial solution for	Background	pH [–]	N_2 [mmol/L]	H_2 [mmol/L]	O_2 [mmol/L]	CH_4 [mmol/L]	CO_2 [mmol/L]	H_2S [mmol/L]	Ar [mmol/L]	Results shown in
Scenario C 20–21 m	BS inflow (Table 3)	5.05	0.849	–	–	–	109	–	–	Figures 15/16
Scenario C 21–22 m	BS inflow (Table 3)	5.03	0.849	–	–	–	114	–	–	Figures 15/16
Scenario C 22–23 m	BS inflow (Table 3)	5.01	0.849	–	–	–	120	–	–	Figures 15/16
Scenario C 23–24 m	BS inflow (Table 3)	4.99	0.849	–	–	–	125	–	–	Figures 15/16
Scenario C 24–25 m	BS inflow (Table 3)	4.97	0.849	–	–	–	130	–	–	Figures 15/16
Scenario C 25–26 m	BS inflow (Table 3)	4.95	0.849	–	–	–	135	–	–	Figures 15/16
Scenario C 26–27 m	BS inflow (Table 3)	4.94	0.849	–	–	–	140	–	–	Figures 15/16
Scenario C 27–28 m	BS inflow (Table 3)	4.92	0.849	–	–	–	146	–	–	Figures 15/16
Scenario C 28–29 m	BS inflow (Table 3)	4.91	0.849	–	–	–	151	–	–	Figures 15/16
Scenario C 29–30 m	BS inflow (Table 3)	4.89	0.849	–	–	–	156	–	–	Figures 15/16

1.1 atm representing the bottom of the columns where heating up of the inflowing water was located by temperature monitoring. After that, the ratio of gas-phase formation per litre water was computed under equilibrium conditions. This comparison was then used to discuss plausibility of the experimental results and the predictability by using geochemical equilibrium modelling.

The inflow solution BS was equilibrated at 10 °C with (a) the atmospheric partial pressures of N_2, O_2, Ar and CO_2 to simulate no changes in dissolved gas concentrations during infiltration of recharge water through the vadose zone of an aquifer and (b) the atmospheric partial pressures of N_2 and Ar, while, according to Matthes (1990), the partial pressure of CO_2 was increased to 0.05 atm and the partial pressure of O_2 was decreased correspondingly to simulate a use up of O_2 and production of CO_2 by aerobic respiration during infiltration. The temperature of these initial solutions (Table 4) was then increased to 25, 40, 55, 70 and 85 °C in a total pressure range from 1 to 2.6 atm to investigate whether a gas-phase formation takes place under these physical and geochemical conditions.

For a first set of initial solutions, pure water was set to equilibrium with a pure atmosphere of each of the gases H_2, N_2, O_2, CH_4, CO_2 and H_2S at 10 °C for total pressures varying from 1 to 10 atm to investigate the effect of an increasing pressure on the formation of a gas phase. Saturated conditions were used to simulate a source for the dissolved gases as e.g. microbial degradation processes or upward gas migration from deeper layers. Either solely the gas corresponding to the dissolved one or alternatively, additionally also water vapour was allowed to partition into the gas phase to determine whether water vapour needs to be considered for calculating the gas-phase formation in the subsequent scenario calculations. In a second set of initial solutions, the dissolved concentrations of H_2, N_2, O_2, CH_4, CO_2 and H_2S were adjusted in 30 steps from 1/30 up to saturation at constant 2 atm total pressure in pure water to compare the saturations of dissolved gases and therefore dissolved gas concentrations causing the onset of a gas-phase formation under specific temperature and pressure conditions. For CO_2, additionally calcite-buffered water was used to demonstrate the dependency of CO_2 solubility and potential gas-phase formation on the buffering capacity and thus pH of an aquifer. For both sets of initial solutions (Table 4), it was then again calculated for temperatures between 25 and 85 °C if a separated gas phase is forming and which volume such gas phases would have.

Scenario calculations

The effects of a temperature-induced gas-phase formation on water and gas-phase saturation and subsequently hydraulic conductivity were investigated by scenario

calculations representing future heat storage sites under different physical and geochemical boundary conditions. For a first scenario A, the groundwater composition in the BS aquifer including 23.8 mg/L of N_2 (which corresponds to an equilibrium with a pure N_2 gas phase at 10 °C and 1 atm) was used to imply an aquifer fed by water that has been in equilibrium to the atmosphere first, but from which oxygen has been consumed and nitrogen has been enriched by degradation of organic carbon via nitrate reduction during infiltration (Table 4). In a second scenario B, the groundwater of scenario A was used as background and methane was chosen as an additional dissolved gas as it might be present in the subsurface due to methanogenic degradation processes (e.g. Amos et al. 2005; McIntosh et al. 2014) or gas leakages out of leaky production (or storage) wells (e.g. Van Stempvoort et al. 2005) in considerable amounts. The methane concentrations increased by depth as due to the assumption of a source, saturated dissolved gas conditions were presumed (Table 4). Methane concentrations corresponding to 30–100% in situ dissolved gas saturation in bedrock wells but also in surficial aquifers overlying organic-rich shale-bearing formations were e.g. measured by McIntosh et al. (2014). The third scenario C again used the groundwater composition from scenario A as background. For this scenario, CO_2 (which has a solubility more than a magnitude higher than e.g. N_2 or CH_4) was chosen as a dissolved gas in addition to N_2. The dissolved gas concentrations were again set to match saturation (Table 4), as comparable to scenario B, an existing CO_2 source was assumed. Such a source might be natural upward migration of gaseous CO_2 from deeper layers along fault zones into shallower regions. The CO_2 can dissolve into the groundwater on its migration pathway and causes soil gas compositions with over 90% CO_2 as it has been observed by

e.g. Chiodini and Frondini (2001), Beaubien et al. (2003), Shipton et al. (2005) and Battani et al. (2010). For the interpretation of the results of these three scenarios, it should be taken into account that only scenario A covers a common situation. For scenarios B and C, additional processes which increase dissolved gas concentrations up to saturation are assumed which only represents the upper end of possible dissolved gas concentrations at ambient groundwater temperatures.

To predict the potential development of a case application based on the three postulated scenarios, we used the numerical heat storage model of Popp et al. (2015) that simulates seasonal heat storage with a field of 72 BHEs heated to a maximum temperature of 60 °C in a near-surface aquifer. Further, the authors assumed a background groundwater temperature of 10 °C and a flow velocity of 0.02 m/d. Correspondingly to Popp et al. (2015), the horizontal extension of the field of BHEs perpendicular to the groundwater flow was assumed to be 18 m. Total pressures were set to 1–2, 2–3 and 3–4 atm simulating heat storage sites in water-saturated depths of 0–10 m for scenario A, 10–20 m for scenario B and 20–30 m for scenario C. The particular depths were chosen in a way that each scenario is located within a sensitive depth range (e.g. scenario A would not cause any gas-phase formation in depths >10 m) and that the calculations do not cause any errors in computation (as e.g. scenario C did in shallower depths). Maximum residual gas-phase saturation (S_{grm}) in the zone of gas-phase formation is reported to remain between 20% (Istok et al. 2007) and 50% (Ye et al. 2009), so the onset for an upward migration of further generated gas phase was set to (a) 30% and (b) 50% gas-phase saturation in the further calculations. The scenario area was divided into five

Fig. 2 Temperature profile of a numerical heat storage model developed to simulate seasonal heat storage in a near-surface aquifer divided up into five sections (S_1–S_5) to calculate gas-phase formation in the three scenarios stepwise for the corresponding increase in temperature (after Popp et al. 2015)
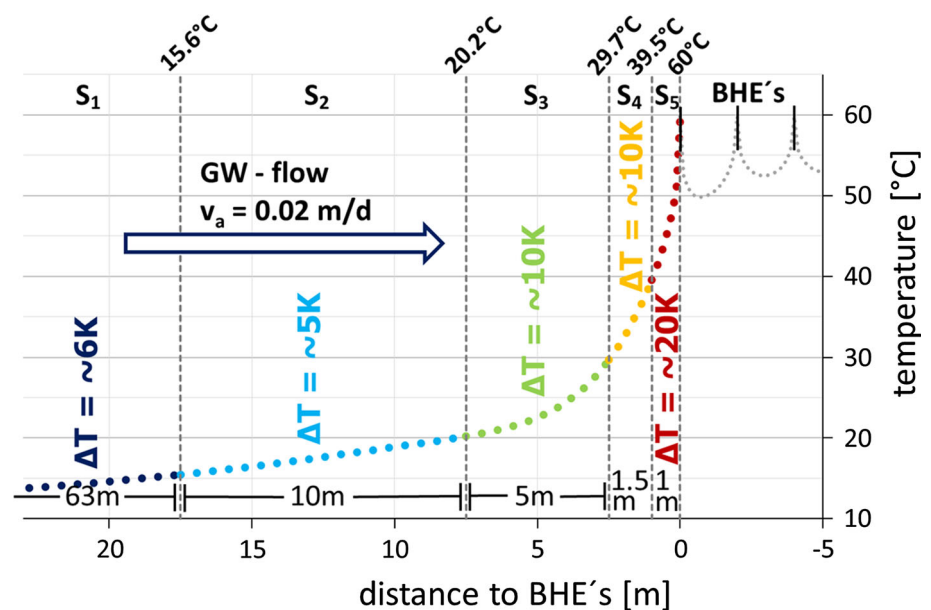
sections (marked as S_1, S_2, S_3, S_4 and S_5 in Fig. 2) in the upstream flow of the heat storage site (which is marked by BHEs for borehole heat exchangers in Fig. 2) where the temperature is elevated above the background aquifer temperature of 10 °C due to conductive heat transport to account for the lateral differences in gas-phase formation.

Formation of a gas phase was subsequently calculated in each of the five sections (S_1–S_5) over time given in exchanged pore volumes for each of the three scenarios' solutions (Table 4). The model of Popp et al. (2015) yielded a stepwise increase in temperature from 10 to 15.6, 20.2, 29.66, 39.52 and 59.86 °C for the selected extent of the five sections (see Fig. 2). For each metre in depth, the corresponding total pressure was used. A gas phase formed and the dissolved gas concentrations decreased correspondingly in case partial pressures of the dissolved gases exceeded the total pressure in a temperature step at any depth, before the solution was used in the next temperature step. The amount of gas phase formed in moles(gas)/L(water) was converted to volume(gas)/L(water) by using ideal gas assumptions. In the appropriate cell (defined by temperature step and depth), the water saturation was then reduced by this factor. After gas-phase saturation reached a S_{grm} of 30 or 50%, further gas-phase formation was not effecting water saturation as an upward migration of this gas phase was assumed. This excess gas phase was then summed up for the whole volume of a section (11,340, 1800, 900, 270 and 180 m³ for the five sections (S_1–S_5), respectively) over time. Under confined conditions, as suggested for ATES sites (e.g. Schmidt and Müller-Steinhagen 2005), gas phase exceeding S_{grm} will migrate upwards and accumulate in morphological traps at the top of the aquifer. Subsequent effects in the field of BHS on heat conductivity (Eq. 9) and heat capacity (Eq. 10) due to changes in the water saturation were calculated for a case scenario assuming all excess gas phase produced upstream of the BHE is being laterally transported into the heat storage field by the groundwater flow.

$$\lambda_{bulk} = \lambda_{sediment} \cdot (1 - n) + \lambda_{water} \cdot (n - n_{eff} + n_{eff} \cdot S_w)$$
$$+ \lambda_{gas} \cdot n_{eff} \cdot S_g \tag{9}$$

$$c_{V_{bulk}} = c_{V_{sediment}} \cdot (1 - n) + c_{V_{water}} \cdot (n - n_{eff} + n_{eff} \cdot S_w)$$
$$+ c_{V_{gas}} \cdot n \cdot S_g \tag{10}$$

For these calculations, volumetric heat capacity (c_v) and heat conductivity (λ) data from Pannike et al. (2006) for a fine-grained sand ($c_v = 2.5$ [MJ/(m³ K)], $\lambda = 2.2$ [W/(m K)]) and from Lide (2005) for water at 60 °C ($c_v = 4.1$ [MJ/(m³ K)], $\lambda = 0.65$ [W/(m K)]) and gases at 27 °C ($c_v = 0.0013$ [MJ/(m³ K)], $\lambda = 0.026$ [W/(m K)]; averaged over water vapour, nitrogen and methane) were used. The porosity (n) for a fine-grained sand ($n = 0.4$) was taken from Pannike et al. (2006), while for effective porosity (n_{eff}) the value ($n_{eff} = 0.1$) given in Popp et al.

(2015) was used. Data for water (S_w) and gas-phase saturation (S_g) resulted from the scenario calculations.

Frequency of pore water replacement is a crucial factor for estimations on the temporally evolution of the gas-phase saturation in the pore space. The frequency of pore water replacement can be calculated and converted into years of operational runtime by using the groundwater flow velocity of 0.02 m/d (as used by Popp et al. 2015) and the given lateral extent of the five sections stated above. By doing so, the number of computations is increasing with a decreasing lateral extent of the sections which results in the varying number of datapoints in the scenario calculations 30-year runtime (Figs. 11, 13, 15). Gas-phase formation was only considered for half the year as a seasonal heat storage site is assumed. Back dissolution in the other half of the year was not included in the calculations. The cumulative changes in water saturation were calculated for an operational runtime of 30 years. According to Amos and Mayer (2006), an approach for the unsaturated zone (Eq. 11; van Genuchten 1980) was used to calculate the resulting change in hydraulic conductivity.

$$K_r(S) = S^{1/2} \cdot \left[1 - \left(1 - S^{1/m}\right)^m\right]^2 \quad \left(m = 1 - \frac{1}{n}\right) \tag{11}$$

Here, K_r is the relative hydraulic conductivity, S the water saturation, m a fitting parameter calculated from n and n a grain size-dependent, dimensionless fitting parameter of water retention which was taken from Schroth et al. (1996) for a medium-grained sand. This approach was shown to be also suitable for gas entrapment into former water-saturated zones by Fry et al. (1997). In addition, the temperature influence on the changes in hydraulic conductivity by viscosity and density changes in the water was included in the calculations. Feedback of changes in the hydraulic conductivity on the groundwater flow was only considered in terms of the reduced water saturation, while the flow velocity was maintained. Focused or deflected flow into areas with elevated or reduced hydraulic conductivity on the vertical axis was neglected.

Results

Gas-phase formation and accumulation in the column experiments

Averaged over the heating period, ~ 100 mL (10 °C), ~ 280 mL (25 °C), ~ 530 mL (40 °C) and ~ 450 mL (70 °C) of residual gas phase remained inside the BS columns which corresponds to a gas-phase saturation of 5, 13, 25 and 21%, respectively (Fig. 3a). For the column operated at 10 °C, no separate gas phase was expected to develop, but gas-phase entrapment at the start of the
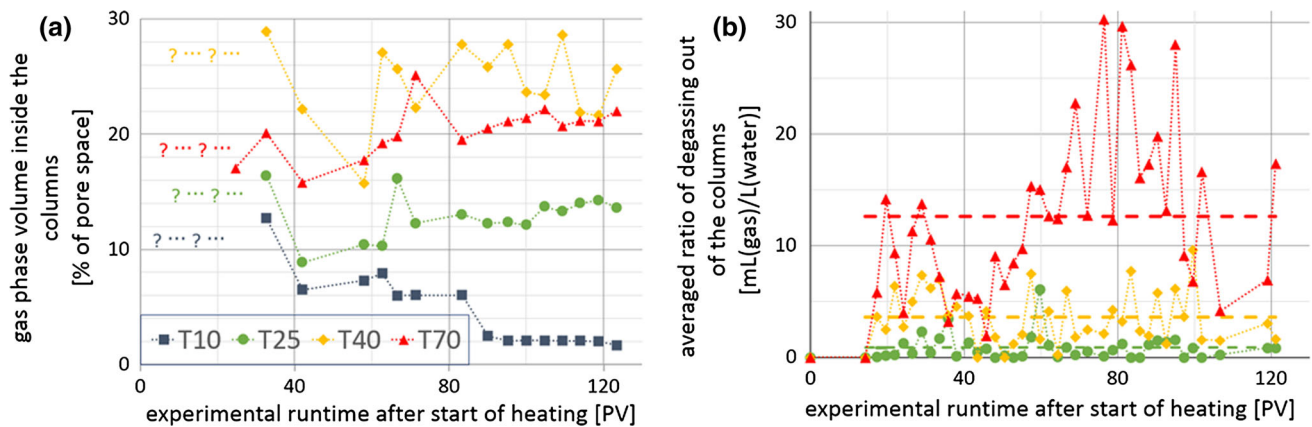
Fig. 3 Accumulated gas phase inside the sediment (a) and averaged ratio of gas phase flushed out as bubbles (b) for the BS columns displayed over the experimental runtime in exchanged pore volumes after heating of the columns was started

experiments (see "Monitoring of gas-phase formation by geoelectrical measurements" section) led to the detection of a gas phase which volume was decreasing by experimental runtime (Fig. 3a). The inflowing water with a total gas pressure of 1.1 atm (Table 3) is heated up within the first 10 cm of the columns; consequently, also the geoelectrical resistance measurements first showed the build-up of a residual gas phase in the lowest measurement segment covering this zone of gas-phase formation (see "Monitoring of gas-phase formation by geoelectrical measurements" section). Accumulation of a gas phase within the zone of gas-phase formation was also observed in column and tank experiments (Istok et al. 2007; Ye et al. 2009). These studies also report a subsequent channel build-up for upward gas migration in case S_{grm} is exceeded locally. The volume of entrapped gas phase at 25, 40 and 70 °C in the experiments done within this study was slightly varying over time which can be explained by build-up of channels for upward gas migration, partial degassing and possibly collapse of some existing channels at times, followed again by the build-up of new channels, when further gas phase was generated. Part of the gas phase that migrated upwards accumulated at the top of the columns as resistivities were increased in the highest monitored part of the column heated to 40 °C (see "Monitoring of gas-phase formation by geoelectrical measurements" section). No electrodes covered the uppermost part of the columns (see Fig. 2), so also at 25 and 70 °C accumulation of a gas phase at top of the columns might have occurred. Enhanced upward migration of gas bubbles compared to natural lateral flow conditions cannot be excluded as these column experiments were conducted with an upward water flow. Thus, the residual gas phase that remained inside this sediment was possibly lower than it could be expected under natural lateral flow conditions. In the BS column experiments, an averaged gas-phase formation ratio of $\sim$1, $\sim$4 and 12 mL(gas)/L(water) was measured for 25, 40 and

70 °C over the experimental runtime (Fig. 3b). The higher ratio of gas-phase formation at 70 °C compared to 40 °C might have caused an enhanced build-up of channels for upward gas-phase migration at 70 °C and thus resulted in a smaller gas volume trapped within the sediment. A limited channel build-up at lower temperatures was also observed by Krol et al. (2011).

The amount of gas phase trapped inside the BS columns showed less variation from 90 exchanged PV onwards (Fig. 3a), so the gas phase flushed out of the columns for comparison with the calculated gas-phase formation was measured from there on. For the OR columns, the gas phase flushed out of the columns was measured for a period of 12 exchanged PV (18 days) without interruption by measurements from 125 exchanged PV onwards when the ratio of degassing had reached a stable value.

By using the inflow solutions compositions, the gas-phase formation in five out of six column experiments is assessable with an uncertainty factor of less than 2 (OR 25, 40, 70 °C and BS 40, 70 °C). The deviation between calculated and measured gas-phase formation ratio is <2.5% at 70 °C where the highest gas-phase formation ratios within this study occur (Fig. 4). Calculated gas-phase formation in the column experiment OR 40 reproduces the slope of measured gas-phase formation between 127 and 137 PV, while the overall deviation is due to two abrupt increases in gas-phase release. The overall deviation in the BS 25 and 40 °C column experiments is too large to be fully explained by retention of gas phase within the grain structure, as this would be clearly visible in Fig. 3a, though it might explain a part of the observed deviations. In addition, work needed to be brought up for formation of a gas-phase embryo is possibly reducing the gas-phase formation at lower temperatures as the chance of successful nucleation increases with supersaturation which corresponds to temperature in this case (Debenedetti 1996).
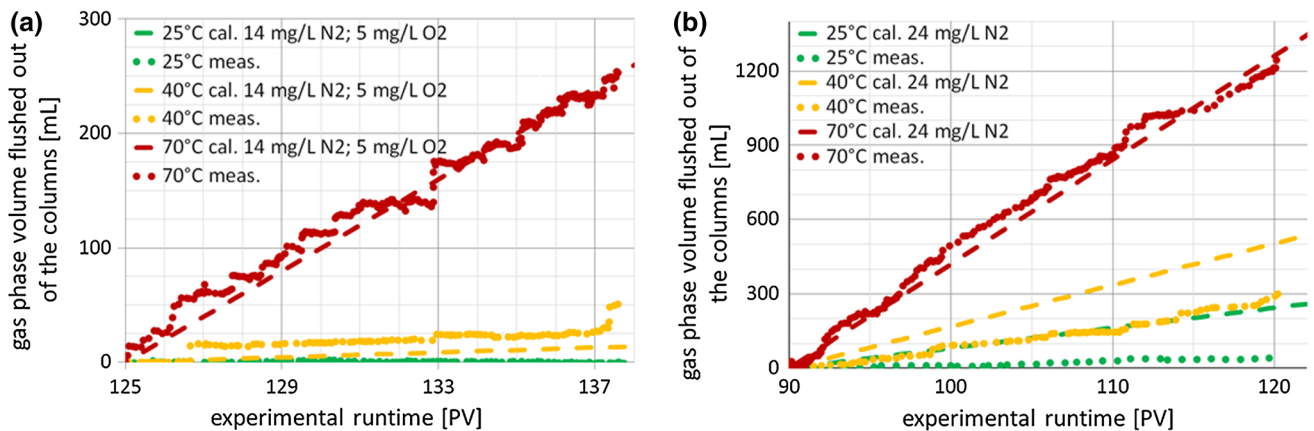
Fig. 4 Comparison between measured and calculated degassing for the OR (**a**) and BS (**b**) column experiments by using measured degassing from 125 (**a**) and 90 PV (**b**) onwards and the composition of the corresponding inflow solution as input parameters for the calculations
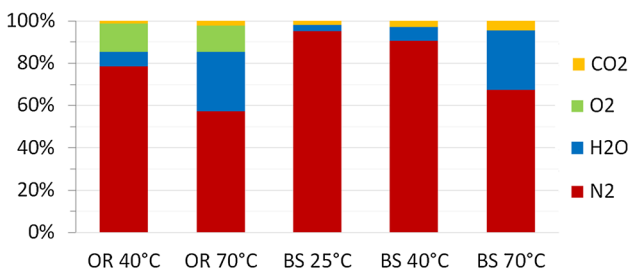

Fig. 5 Composition of the calculated gas phases for the OR and BS column experiments

The calculated gas-phase formation for comparison with the measured one has been computed on the bases of the inflow solutions without consideration of any sources or sinks for dissolved gases within the columns. The calculated gas phases contain between 57 (OR 70 °C) and 95% (BS 25 °C) of nitrogen whereupon the share of nitrogen decreases towards higher temperatures (Fig. 5). In contrast, the share of water vapour increases from 3% at BS 25 °C to 18% at BS 70 °C. Oxygen, although on a smaller scale, shows a pattern similar to nitrogen as its share also decreases with temperature from 14 (OR 40 °C) to 12% (OR 70 °C). In contrast, the share of CO_2 increases with temperature but is restricted to a maximum of 5% (BS 70 °C; Fig. 5). Partition of N_2 or water vapour into the gas phase will not cause considerable changes in the fluid phase' characteristics. In contrast, degassing of O_2 can facilitate the development of reducing conditions by removing a possible electron acceptor from water. Calculation of the calcite saturation index showed an increase in calcite oversaturation by 1, 1.7 and 2.1% due to CO_2 degassing in the BS columns heated to 25, 40 and 70 °C compared to heating without considering gas-phase formation (not shown). The compositions of the gas phases would be shifted towards CO_2 and N_2, H_2S or CH_4 in case OC degradation would be considered (not shown).

Monitoring of gas-phase formation by geoelectrical measurements

The base measurements of the electrical behaviour for the BS columns started on Sunday, the 8 November 2015. However, the groundwater circulation was started 2 days later at the 11 November. Figure 6a illustrates the variation of the electrical bulk resistivity during the 2 months of the baseline monitoring. Without groundwater flow, the measured resistivities were very low and varied in the differing measuring segments (from 40 to 70 Ωm) without significant relation to the column heights. In each column, increased resistivity values (70–85 Ωm) were observed in the lowest segment of the columns. Since these anomalies disappear after the start of perfusion with water, these values cannot be explained by the special commercial quartz in the lowest centimetres of the columns. Moreover, this indicates gas-phase entrapment particularly at these regions while filling the columns. After the start of percolation with groundwater from the bottom to the top of the columns, the resistivities increased up to 80–120 Ωm. Resistivity increases of the upper column segments lag systematically behind those of lower column segments. This suggests a differing chemical composition of the groundwater in contrast to the filled columns with the saturated sediment. The high values above 140 Ωm (up to approximately 600 Ωm) in the lowest measurement segment of the first column (Fig. 6a, 10 °C) at the 13–28 November lead to the suggestion of gas-phase infiltration with the groundwater flow. Using Eq. 6 leads to the suggestion of a gas-phase saturation of almost 65%. Indeed, the gas phase is transported upwards with the groundwater flow illustrated by the red to orange fan in Fig. 6a (10 °C). At the end of the baseline measurements, almost equal resistivity values indicating equal temperature and measurement conditions with an almost homogeneous sediment infill were found.
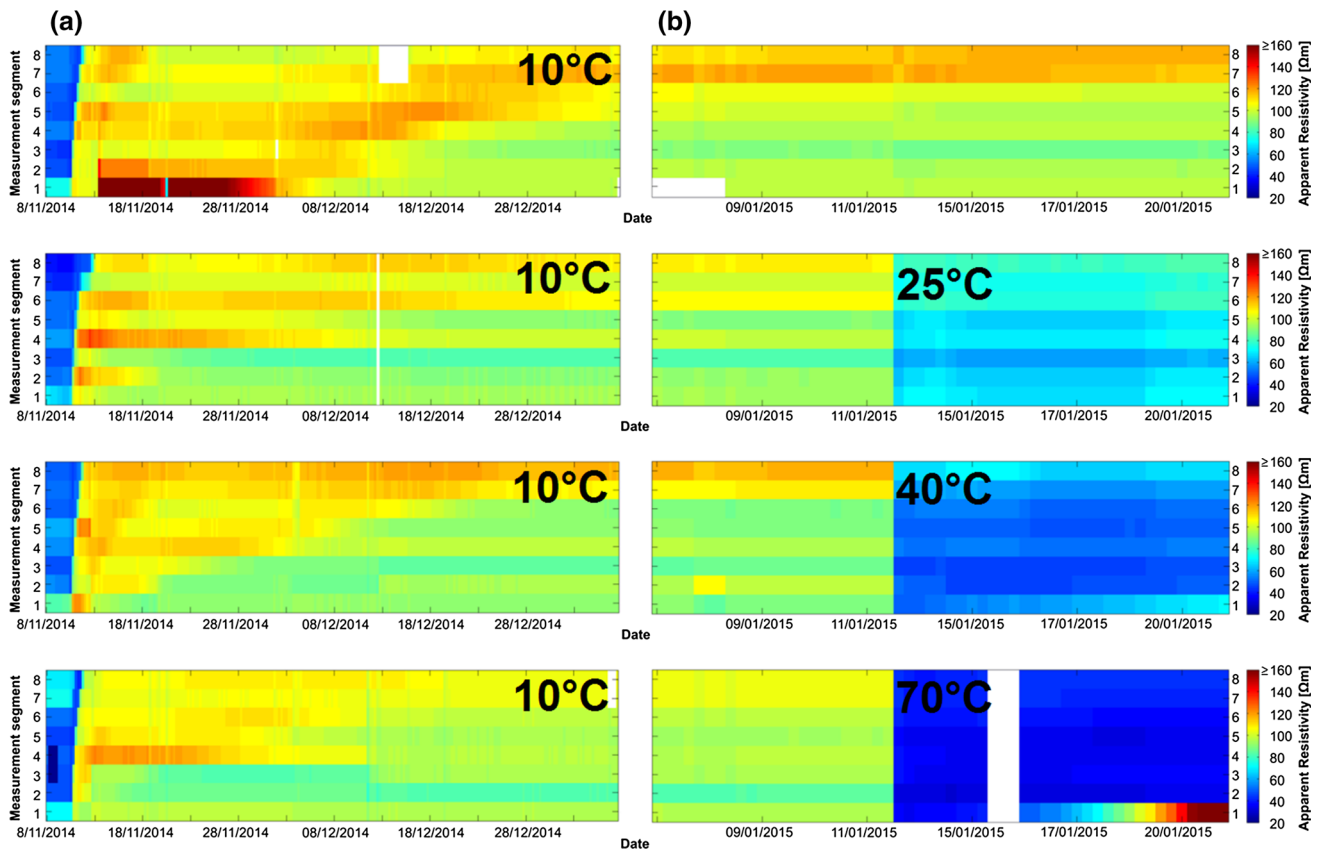
Fig. 6 Electrical resistivity results of each of the *four columns* in the first 2 months in the freezer at a temperature of 10 °C. After the first 3 days with relative low electrical resistivity results (between 60 and 80 Ωm), the switch on of the groundwater circulation induced an increase in the resistivity values up to 110 Ωm (**a**). Electrical resistivity results of each of the *four columns* in the switchover of the baseline monitoring to the heating phase (**b**). Erroneous values are *coloured white*

Figure 6b shows the transition from the baseline monitoring to the heating process of the three columns (Fig. 6b, 25, 40 and 70 °C) and the reference column remained at 10 °C (Fig. 6b, 10 °C). The heating process started at the 13 January. For the necessary technical installations and reorganisation of the columns, the measurements had to be interrupted 1 day before. Already the first measurements after the interruption show that the resistivities were affected by the temperature changes (Fig. 6b). Since no significant resistivity variations over time and segment height, analogue to those observed after starting the water circulation, were observed, the heating process was proven to be fast and affected the columns equally. The resistivities decreased proportional to the different temperature values in each column. While the resistivity values for the column at 25 °C decreased down to 70–80 Ωm, the values for the column at 40 °C decreased down to 50 Ωm and for the column at 70 °C down to 40 Ωm, approximately (Fig. 6b). To prove the influence of the temperature and to exclude possible gas-phase influence, the measured values of the first 2 days after starting the heating period were compared to the model of Dachnov (1962) (Eq. 4).
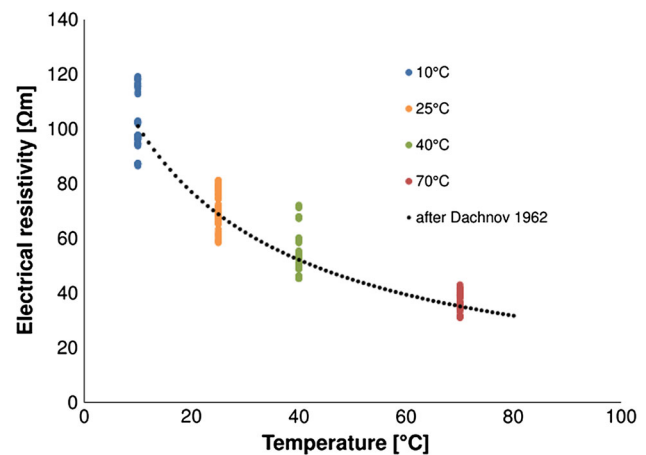

Fig. 7 Measured resistivity values of the four columns of every segment in the differing heights from 13 to 14 January in comparison with the calculated values based on the model of Dachnov (1962)

Figure 7 shows all measured values from 13 to 15 January, over the whole range with its minimum and maximum values, for all four columns (10, 25, 40 and 70 °C) and the values calculated based on Dachnov (1962). Even with the

outliers in the segments at the top of the column at 10 and 40 °C (Fig. 7), the plotted measured values show a good agreement with the calculated values according to the model of Dachnov (1962).

However, anomalies were found in the lowest measurement segment in the column heated up to 70 °C starting at the 17 January (Fig. 6b 70 °C). Since these high ER values reach up to 200–500 Ωm, these anomalies cannot be explained by the temperature influence anymore. Consequently, there must be changes in the pore filling such as displacement of the pore water by gas-phase formation. Thus, based on Eq. 6 a gas-phase saturation of 55–70% was calculated for this measurement segment depending on the measured resistivity values. In the column heated up to 40 °C, little anomalies were found starting in the end of January, and high anomalies with similar values (150–350 Ωm) analogue to the lowest segment of the column at 70 °C were found at the end of March. Corresponding to Eq. 6, we found a gas-phase saturation between 40 and 60% varying over time based on the measured resistivity values. In the lowest segment of the column heated up to 25 °C, smaller anomalies (up to 150 Ωm) have been observed starting in June (Fig. 8, 25 °C). Here, a gas-phase saturation of approximately up to 25% was calculated.

Moreover, after the first occurrences of these anomalies in each column, the high ER values did not persist constantly. Figure 8 illustrates the behaviour of the ER of the columns from 5 February until 6 March and later in June. The changes in the ER in the lowest measurement segment proceed heterogeneously instead of a continuous drift leading to the suggestion of outgassing phases. Since these changes occur almost simultaneously over the entire term of the experiment (here only presented for the stated time from February to March and June, cf. Fig. 8), a manual impulse based on the water sampling can be assumed. However, the measured values in the segments above do not represent similar anomalies that would indicate a drift of the gas fraction towards the upper measured segments as we could observe for in the base measurements with the illustrated fans (Fig. 6a).

Based on the assumption that gaseous bubbles should migrate upwards and accumulate at the top of the columns, higher resistivity values in the upper measurements segments should be monitored from time to time compared to the central measurement segments. Occasionally, in the upper measurement segment of the column at 40 °C increased resistivity values have been observed (Fig. 8 40 °C, June). In response to Eq. 6, for the upper segment a gas-phase saturation of approximately 15% was calculated. This effect was not measured at the other columns. However, as introduced in the "Materials and methods" section (and cf. Fig. 1) based on the arrangement of the cannulas,

the most upper 15 cm of the columns could not be monitored by the electrical measurements. Thus, the results here give no information about possible gaseous accumulation in the upper segments of the columns as given in the literature (Istok et al. 2007; Ye et al. 2009).

Calculated gas-phase formation at different pressures, temperatures and dissolved gas concentrations

Formation of a separated gas phase can be expected up to water-saturated depths between 3 and 15 m when the temperature of BS site water in equilibrium with atmospheric N_2, O_2, Ar and CO_2 partial pressures is increased to temperatures between 25 and 85 °C, respectively (Fig. 9a). In case the CO_2 partial pressure of infiltrating water is increased to 0.05 atm due to aerobic respiration, the O_2 partial pressure needs to be reduced accordingly about the same partial pressure to keep the sum of partial pressures below the atmospheric pressure conditions of 1 atm. This leads to a gas-phase formation that extends maximum 1 m deeper for the same increases in temperature (Fig. 9b). Averaged over the whole pressure range, the increase in gas-phase formation due to an increased CO_2 partial pressure in the soil air is more pronounced at lower ($88 \pm 4\%$ at 25 °C) than at higher temperatures ($68 \pm 9\%$ at 85 °C; Fig. 9).

A gas-phase formation at higher hydrostatic pressures may also occur in case the groundwater contains additionally dissolved gases as e.g. H_2S, CO_2, CH_4, O_2, N_2 or H_2. Considering only a single gas component saturated at a particular pressure and temperature and by assuming ideal gas behaviour, a definite temperature increase at constant pressure will lead to the formation of a gas phase with a constant volume, independent from the pressure head. At initial conditions (temperature = T_{ini}, gas pressure = $p(Gas)_{ini} = P_{total}$), the dissolved gas concentration ($c(Gas)_{ini}$ mol L^{-1}) depends on the Henry coefficient and gas pressure (Eq. 12):

$$c(Gas)_{T_{ini}} = K_{H_{T_{ini}}} \cdot p(Gas)_{ini} \qquad (12)$$

Equation 13 describes the dissolved gas concentration after heating and equilibration ($c(Gas)_{end}$ mol L^{-1}):

$$c(Gas)_{T_{end}} = K_{H_{T_{end}}} \cdot p(Gas)_{end} \qquad (13)$$

With $p(Gas)_{end} = p(Gas)_{ini} = P_{total}$, the variation of the dissolved gas concentration ($\Delta c(Gas) = c(Gas)_{ini} - c(Gas)_{end}$) is calculated by Eq. 14:

$$\Delta c(Gas) = \Delta K_H \cdot P_{total} \qquad (14)$$

The amount of molecules portioning into the evolving gas phase ($n = -\Delta c(Gas)$) is linearly related to the partial
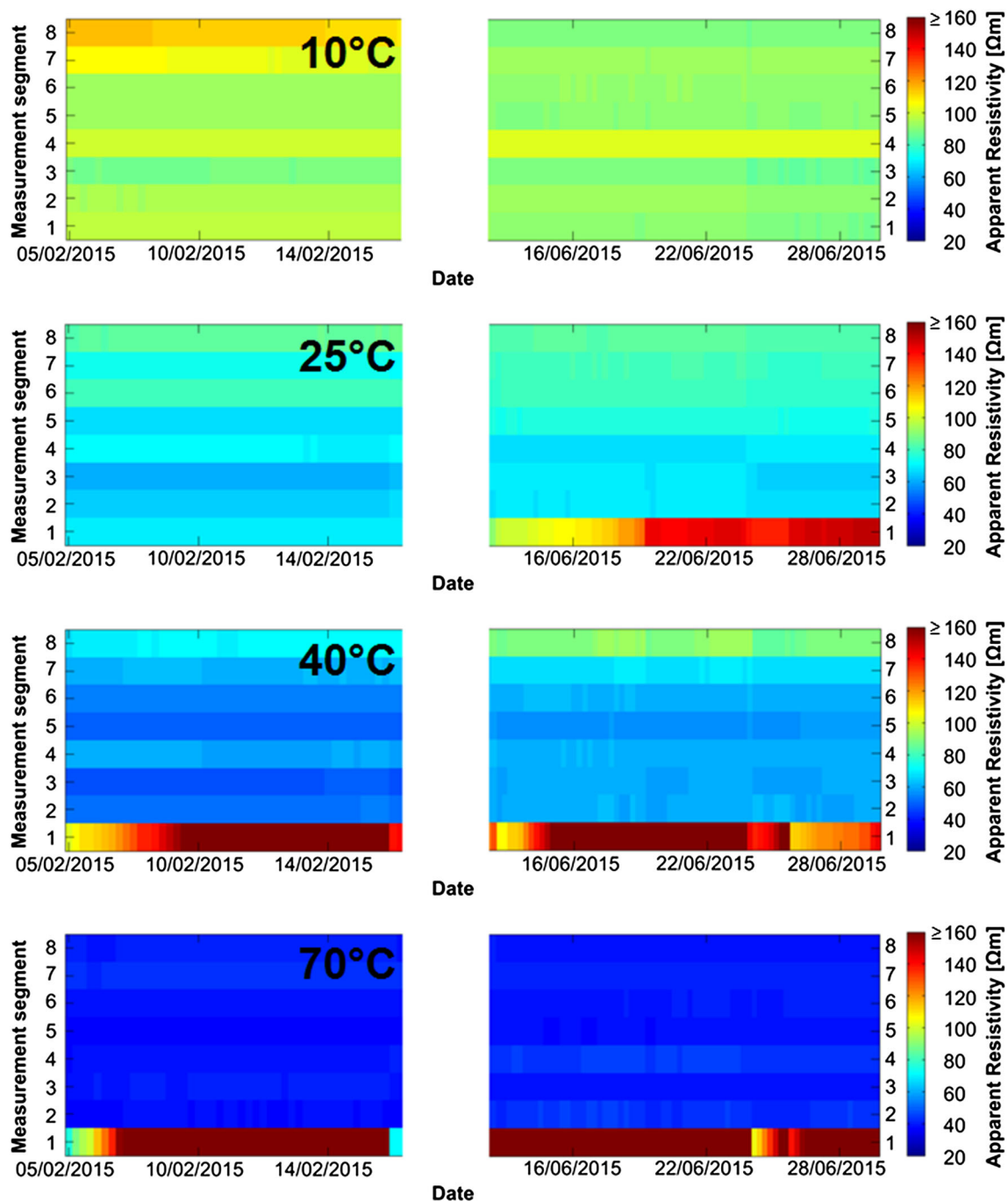
Fig. 8 Measured resistivity values of the four columns from 5 to 16 February and from 14 to 29 June. The data present the variation of these anomalies during the experiment. These anomalies started in column set to 40 and 70 °C already in January, while the anomalies for the column set to 25 °C were first registered in the middle of June.

Further, the data present the increased resistivity values in the upper measurement segment of the column set to 40 °C in the end of the experimental runtime corresponding to the assumption of an accumulation of the gas bubbles at the *top of the columns*

pressure (=total pressure) and also linearly related to the difference in the Henry coefficients (ΔK_H) for the examined temperature increase. Thus, the number of moles in the evolving gas phase is related to the solubility as well as to the reaction enthalpy, both combined defining the ΔK_H.

At a particular ΔT, the ΔK_H remains constant and therefore the number of moles entering the gas phase becomes only related to the partial pressure (=total pressure). Using the ideal gas law for calculating the gas volume yields (Eq. 15):
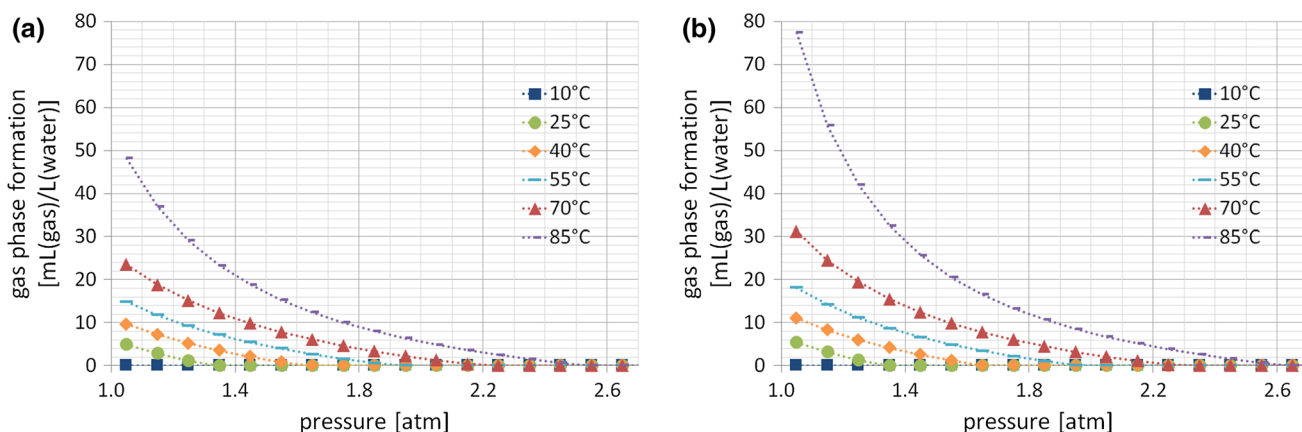
Fig. 9 Calculated gas volume at temperatures up to 85 °C and total pressures between 1 and 2.7 atm for near-surface aquifer conditions represented by BS site water set to equilibrium with atmospheric partial pressures (**a**) or with atmospheric partial pressures but increased CO_2 (to 0.05 atm) and accordingly decreased O_2 (to 0.16 atm) partial pressures (**b**), whereby the initial total gas pressure was 1 atm in (**a**) and (**b**)
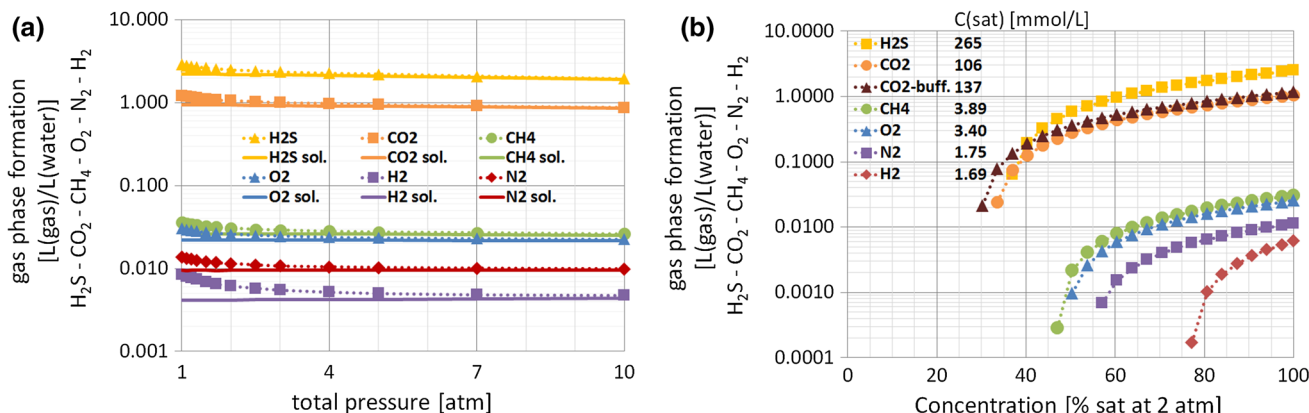

Fig. 10 Influence of gas-phase assemblage and pressure conditions (**a**) and dissolved gas concentrations at a fixed total pressure of 2 atm (**b**) on the formation of a separate gas phase in L(gas)/L(water) exemplarily shown for 55 °C (data for 25, 40, 70, 85 °C attached)- *note* uppermost data point in (**b**) represents C(sat) and is equivalent to the 2 atm datapoints in (**a**)

$$V = \frac{n \cdot R \cdot T_{end}}{P} = \frac{-\Delta c(\text{Gas}) \cdot R \cdot T_{end}}{P}$$
$$= \frac{-\Delta K_H \cdot P_{total} \cdot R \cdot T_{end}}{P} = -\Delta K_H \cdot R \cdot T_{end} \quad (15)$$

Equation 15 indicates that the gas volume remains constant over the whole pressure range because of the linear relation between pressure, number of moles and gas volume in the ideal gas law. Overall, the evolving gas volume is mainly related to the gas solubility at these boundary conditions, because of only minor differences in reaction enthalpy. The solid lines in Fig. 10a indicate the evolving single-component gas volume for heating one litre of the initial solution up to 55 °C at constant pressure conditions between 1 and 10 atm. The volume ranges from 0.0041 to 0.025 L(gas)/L(water) for H_2, N_2, O_2 and CH_4, while the one of CO_2 and H_2S ranges from 0.86 to 1.9 L(gas)/L(water), illustrating the importance of the gas solubility for the evolving gas volume. PhreeqC v3.15 (Parkhurst and Appelo 2013) uses the Peng–Robinson

equation of state instead of the ideal gas law for calculating the activity of gases in the gas phase, and this results in a slightly decreasing gas volume at increasing pressure within the considered pressure range between 1 and 10 atm.

The dashed lines in Fig. 10 represent the evolving gas volume in case water vapour is allowed as an additional gas component in the gas phase (Fig. 10a). The gas-phase volume considering water vapour at lower P_{total} increases considerably compared to the single gas-phase case but with increasing P_{total} the difference becomes smaller. Equation 16 describes that the partial pressure of water vapour after heating ($p(H_2O)_{end}$) depends only on the temperature adjusted Henry coefficient ($K_{water, \ T\_end}$), assuming the activity of liquid water is equal to one:

$$\left(K_{water_{T_{end}}} \right)^{-1} = p(H_2O)_{end} \quad (16)$$

Equation 16 indicates that the water vapour pressure is independent from the total pressure. Taking into account

that the partial pressure of the dissolved gas after heating is now $p(Gas)_{end} = P_{total} - p(H_2O)_{end}$, Eq. 13 yields:

$$
\begin{aligned}
c(Gas)_{T_{end}} &= K_{H_{T_{end}}} \cdot p(Gas)_{end} \\
&= K_{H_{T_{end}}} \cdot \left(P_{total} - p(H_2O)_{end} \right)
\end{aligned}
\tag{17}
$$

Equation 17 indicates that the dissolved gas concentration after heating becomes smaller compared to the single gas-phase case because the introduction of the water vapour pressure lowers the partial pressure of the gas phase. Therefore, more molecules of the dissolved gas (H_2S, CO_2, CH_4, O_2, N_2 or H_2) will enter the gas phase and consequently a larger gas volume will establish at equal total pressure. Additionally, water vapour in the gas phase increases its volume, but with a minor effect. Equation 17 shows also that the relative effect of the water vapour on the final partial pressure of the dissolved gas becomes smaller at increasing total pressure. That explains the convergence of the evolving gas volume between the single gas approach and the gas–water vapour approach visible in Fig. 10a. Therefore, the increase in the gas volume, compared to the single gas approach, is highest at 1 atm (47%) and lowest at 10 atm (4.1%).

The effect of allowing water vapour as a gas-phase component on the gas-phase volume is lower at 25 °C [mean increase of 15% (1.5%)] and higher at 85 °C [mean increase of 338% (16%)] at 1 atm (10 atm) due to temperature dependency in water vapour partial pressure (data attached). In the scenario calculations (see "Effects on gas phase saturation and hydraulic conductivity in the zone of maximum residual gas phase saturation (S_{grm}) by scenario calculations" section), water vapour has to be considered as a gas-phase component as the effect cannot be neglected below 4 atm and at temperatures up to 60 °C. In the scenario calculations, a multicomponent gas phase is used due to the initial dissolved gas components whereby including water vapour has an influence on all of the other partial gas pressures.

The onset for the concentration-controlled gas-phase formation of H_2S, CO_2, CH_4, O_2, N_2 and H_2 is at 37, 34, 47, 50, 57 and 77% of the saturation concentration at fixed boundary conditions of 2 atm total pressure and an exemplary temperature increase to 55 °C, corresponding to dissolved gas concentrations of 98, 36, 1.8, 1.7, 1.4 and 0.96 mmol/L, respectively (Fig. 10b). The gas-phase formation for H_2, N_2, O_2 and CH_4 ranges from 0.0002 to 0.031 L(gas)/L(water), while the one of CO_2 and H_2S ranges from 0.029 to 2.5 L(gas)/L(water) (Fig. 10b). The values stated for CO_2 represent the volume of gas-phase formation in an unbuffered aquifer (initial pH of 3.7–4.5). The initial pH is increased to 5.8–6.8, and thus, the solubility of CO_2 at 2 atm is increased from 106 to 137 mmol/L by assuming a calcite-buffered aquifer (CO_2-buff. in

Fig. 10b). The volume of gas-phase formation is between 80 and 12% higher in the buffered system compared to the unbuffered system between 37 and 100% of the saturation concentration, respectively (Fig. 10b). In the calculations for scenario C, CO_2 is dissolved up to saturation and as a northern German, quartz-rich, carbonate-poor aquifer (Table 2) is used as background for the scenario calculations, the unbuffered case was assumed.

Water in equilibrium to atmospheric partial pressures or to a soil air enriched in CO_2 revealed temperature-induced gas-phase formation only in the range of tens of mL gas per L water at its maximum (Fig. 9). To assess potential impacts of such a gas-phase formation, an accumulation of the gas phase with time due to the groundwater flow has to be considered. The volume of a temperature-induced gas-phase formation slightly decreases with pressure (depth) and therefore approaches a stable value due to a diminishing contribution by water vapour, even in case a source leads to saturated dissolved gas concentrations. Hence, the formation of a separate gas phase cannot be excluded solely by the fact of high aquifer pressures without knowledge about the physical and geochemical site conditions.

Degradation of organic carbon or pollutants, which might be intensified at higher temperatures (Bonte et al. 2013a; Jesußek et al. 2013), can increase dissolved concentrations of reaction products as CO_2, N_2, H_2S and CH_4. Threshold dissolved gas concentrations which trigger the onset of a gas-phase formation for N_2 and CH_4 are comparably smaller as for H_2S or CO_2 (Fig. 10b); thus, at sites containing a lot of degradable organic carbon (natural or pollutant), the formation of a separate gas phase can depend on the preferential degradation pathway. In terms of estimating the extent of a gas-phase formation, the predominant degradation process has to be considered temperature dependent as well (Bonte et al. 2013a; Jesußek et al. 2013).

Effects on gas-phase saturation and hydraulic conductivity in the zone of maximum residual gas-phase saturation (S_{grm}) by scenario calculations

In the heat storage model used as background for the scenario calculation, the temperature gradient gets steeper with decreasing distance to the field of BHS (Fig. 2). The ratio of gas-phase formation per litre water follows the temperature gradient and so most of the gas phase forms in the direct vicinity of the BHEs. To account for the lateral differences in gas-phase formation, the scenario field was divided into five sections [S_5 shown in red (closest), S_4 in yellow, S_3 in green, S_2 in blue and S_1 not shown (furthest)]. Within these sections, the gas-phase formation is horizontally averaged. Gas-phase formation in S_1 is distributed over 63 m in flow direction resulting in only six exchanged pore volumes over
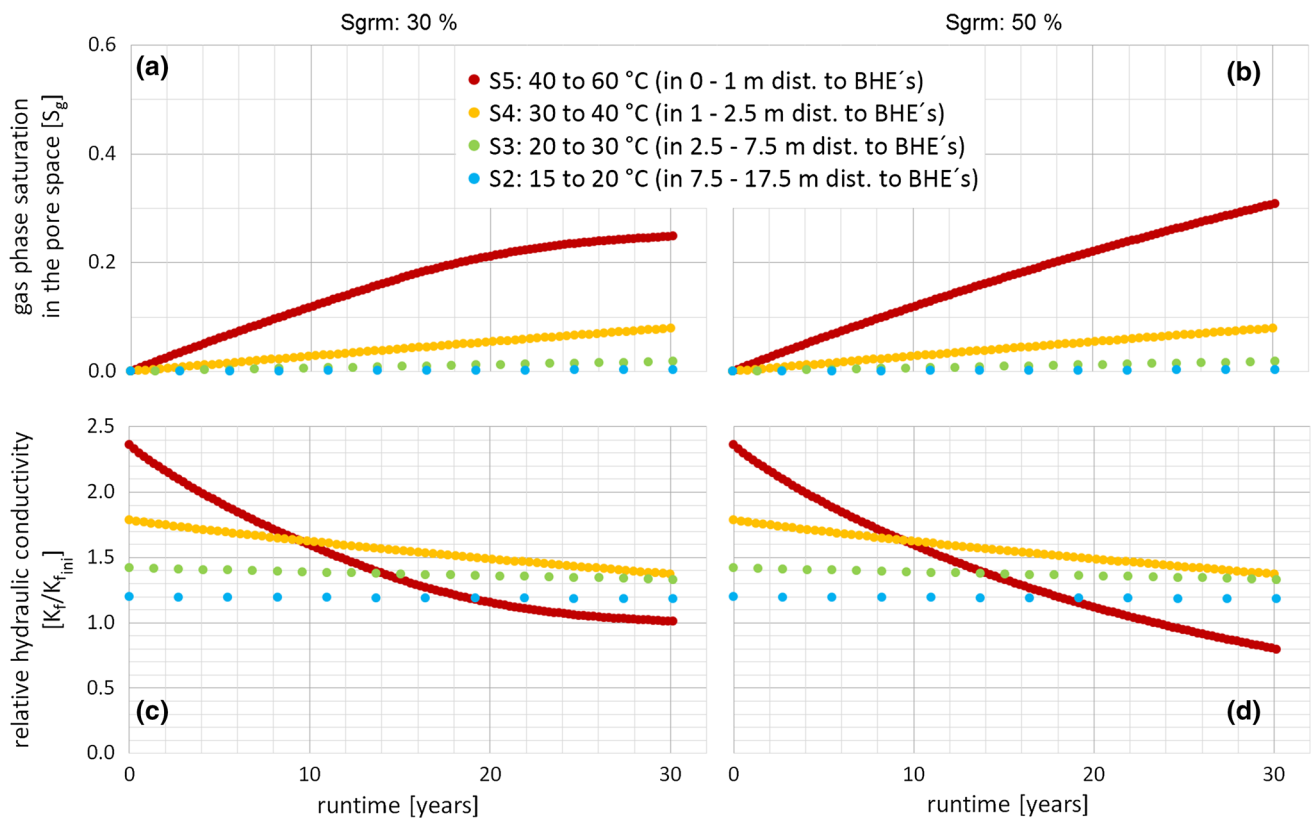
Fig. 11 Development of gas-phase saturation in the pore space (**a**, **b**) and relative hydraulic conductivity (**c**, **d**) averaged over the 10-m-thick aquifer in 30 years of runtime as a seasonal heat storage under conditions of scenario A with a S_{grm} of 30 (**a**, **c**) or 50% (**b**, **d**)

30 years of runtime. The wide extent of this S_1 together with a temperature increase of only 5.5°K leads to a very flat temperature gradient and thus only neglectable effects arise which are not further discussed. Forming gas phase is assumed to accumulate where it is produced due to immobility as long as gas-phase saturation is below the S_{grm}. Further generated gas phase is assumed to horizontally and/or vertically migrate out of the zone of gas-phase formation (see "Effects on gas-phase saturation, heat conductivity and heat capacity in the zone of gas-phase accumulation by scenario calculations" section).

The average gas-phase saturation in S_5 of the 10-m-thick aquifer increases up to ∼25% for a S_{grm} of 30% (Fig. 11a) or ∼30% for a S_{grm} of 50% (Fig. 11b) after 30 years of runtime in case oxygen is consumed and nitrogen is produced up to saturated dissolved gas concentrations under atmospheric pressure conditions by aerobic respiration and nitrate reduction (scenario A). Already in S_4 the gas-phase saturation is less than 10% after 30 years of runtime while the farther away S_3 and S_2 are even less affected (Fig. 11a/b). In S_5, the increase in gas-phase saturation is limited to ∼5% (Fig. 11a/b) within the first 5 years. This results in a decrease in hydraulic conductivity of ∼20% with a remaining hydraulic conductivity still nearly double as high as the initial hydraulic conductivity at 10 °C (Fig. 11c/d).

The depth-averaged hydraulic conductivity remains increased over most of the runtime as the reduced density and viscosity outweigh the decreasing water saturation (Fig. 11c/d). This would lead to an increased groundwater flow velocity in the heated zone (Popp et al. 2015). Hydraulic conductivity in S_5 decreases below the value of undisturbed groundwater at 10 °C only after ∼23.5-year runtime and in case S_{grm} is 50% (Fig. 11d).

The assumption of a vertically homogeneous distribution of the gas-phase formation from the top to the bottom of the 10-m-thick aquifer in scenario A is a simplification. For the most affected S_5, the increase in gas-phase saturation (Fig. 12a/b) and the decrease in hydraulic conductivity (Fig. 12c/d) were therefore additionally calculated depth-specifically. Gas-phase saturation increases up to the assumed S_{grm} of 30% in water-saturated depths of 0–7 m (Fig. 12a). The amount of volume-based gas-phase formation decreases with pressure and depth in a comparable way as it was shown for BS site water equilibrated with atmospheric partial pressures (Fig. 9). As a consequence, with each metre in depth from 0 to 7 m it takes longer to reach a S_{grm} of 30%. At depths between 7 and 10 m, 30% gas-phase saturation is not reached at all within the 30-year runtime (Fig. 12a). Hydraulic conductivity in the upper 7 m decreases below

Fig. 12 Depth specific resolution of changes in gas-phase saturation in the pore space (**a**, **b**) and relative hydraulic conductivity (**c**, **d**) for scenario A with assumed S_{grm}'s of 30% (**a**, **c**) or 50% (**b**, **d**) in S_5; markers in *black* indicate runtime when S_{grm} is reached; markers in *grey* indicate runtime when hydraulic conductivity is equivalent to the initial value at 10 °C
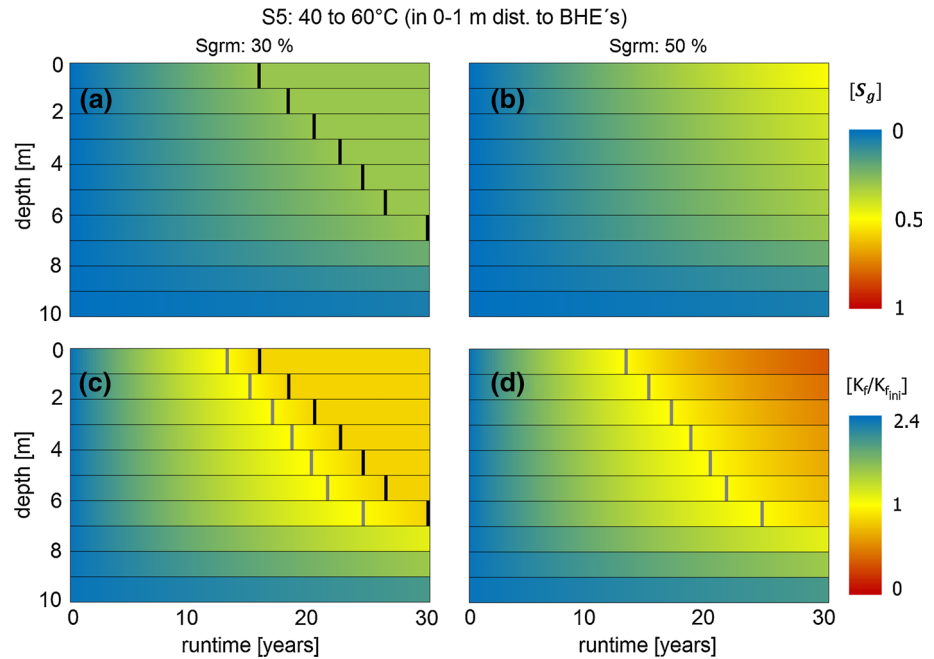
initial values (Fig. 12c/d) which is not apparent from the depth-averaged results in case S_{grm} is 30% (Fig. 11c). Gas phase being generated after S_{grm} is reached will start to migrate out of the zone of gas-phase formation (see "Effects on gas-phase saturation, heat conductivity and heat capacity in the zone of gas-phase accumulation by scenario calculations" section). A S_{grm} of 50% is not even reached at the top of the aquifer within 30-year runtime (Fig. 12b), so probably no or very limited gas-phase migration can be expected in this case.

Nitrogen partial pressures in the soil air are reported to remain about constant on an atmospheric level (Matthes 1990), though the data available (e.g. Andrews et al. 2005) and also the measurements done within this study imply high dissolved concentrations near equilibrium to a pure N_2 gas phase being more the rule than the exception. Already temperatures in a range of 40–60 °C can cause the formation of a separate gas phase to an extent that lowers hydraulic conductivity below initial values, even if no further dissolved gases in addition to N_2 are present in considerable amounts. So especially in near-surface aquifers situated in water-saturated depths of <10 m, as in scenario A, heat storage application design needs to consider the interaction between pressure, operating temperature and dissolved gas concentrations.

If methane is dissolved up to saturation due to the presence of a methane source in addition to dissolved N_2 (scenario B), the average gas-phase saturation in the 10-m-thick aquifer S_5 increases up to assumed S_{grm}'s of 30 or 50% in 14 or 29 years, respectively (Fig. 13a/b). In S_4, gas-phase saturation reaches 24% after 30 years of runtime

(Fig. 13a/b). In this scenario, it lasts 12 and 21 years until the hydraulic conductivity in S_5 and S_4 decreases below the initial hydraulic conductivity (Fig. 13c/d). If the increased hydraulic conductivity due to viscosity and density effects is set as basis, over the whole runtime of 30 years, the depth-averaged hydraulic conductivity decreases about 65 and 86% in S_5 for assumed S_{grm}'s of 30 and 50% (Fig. 13c/d). Gas-phase saturations are limited to 10% or even less in the farther away S_3 and S_2 (Fig. 13a/b). In S_5, gas-phase saturation increases to 11% and hydraulic conductivity decreases by 31% within the first 5 years of runtime (Fig. 13a–d). This corresponds to an intensification of the increase in gas-phase saturation and decrease in hydraulic conductivity of ∼100 and ∼50% compared to scenario A, respectively.

Again, the most affected S_5 closest to the BHEs is further investigated depth-specifically in 1 m units. But differences in gas-phase formation and thus changes in gas-phase saturation and hydraulic conductivity with depth are very limited (Fig. 14a–d) as methane is dissolved up to the dissolved saturation concentration in each depth (under the precondition of the N_2 concentrations of scenario A). This homogeneous gas-phase formation with depth can be traced back to the small changes in temperature-induced gas-phase formation shown for individual gases dissolved up to saturation at total pressures between 2 and 3 atm (Fig. 10a). So the main findings of the depth-averaged calculations for S_5 (S_{grm} is reached after 14 and 29 years, decrease in hydraulic conductivity of 65 and 86%, both for a S_{grm} of 30 and 50%, respectively; Fig. 13a–d) also apply for each specific depth (Fig. 14a–d). Gas phase generated
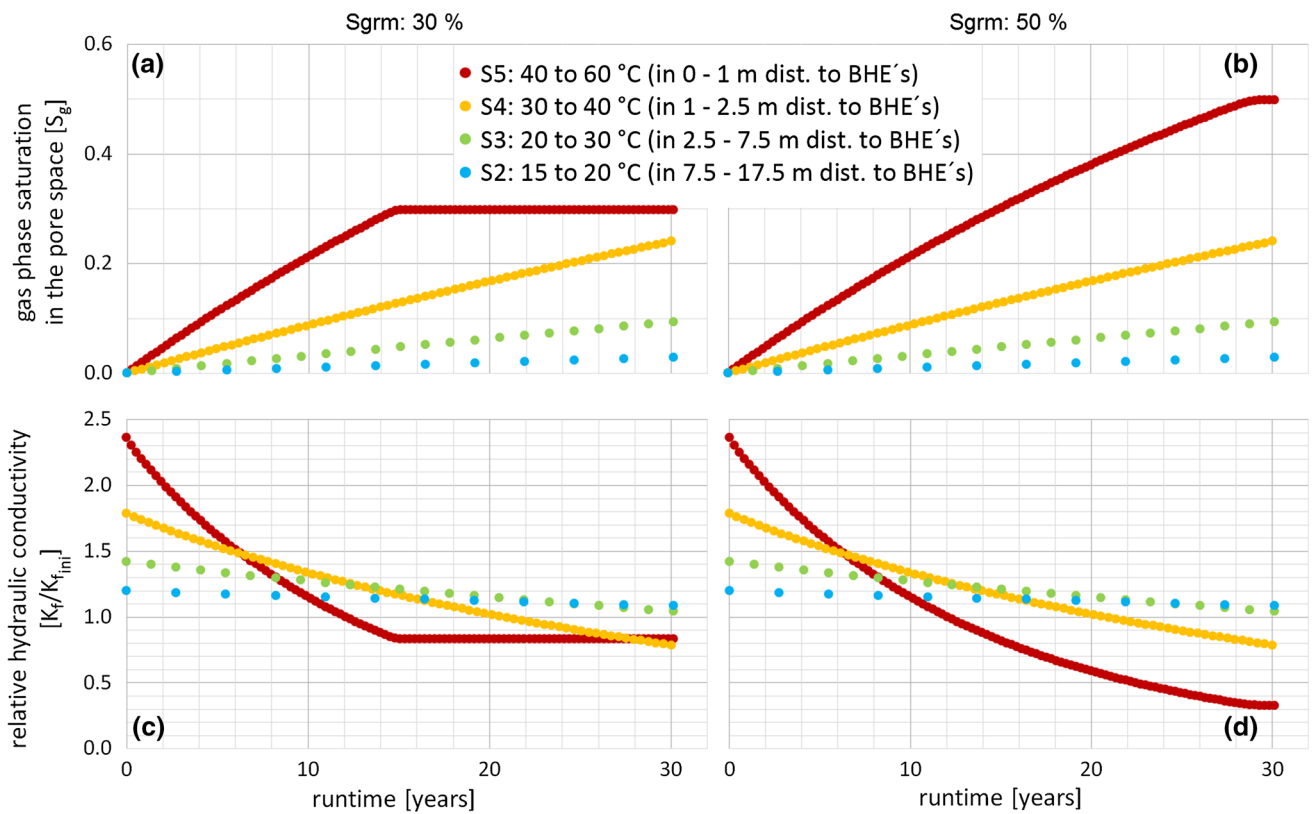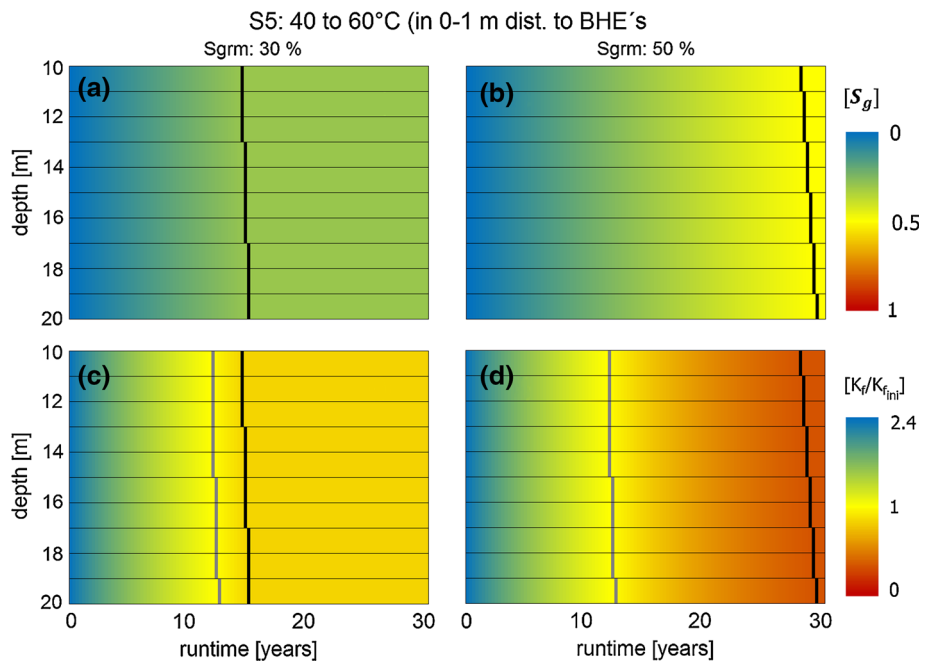
Fig. 13 Development of gas-phase saturation in the pore space (**a, b**) and relative hydraulic conductivity (**c, d**) averaged over the 10-m-thick aquifer in 30 years of runtime as a seasonal heat storage under conditions of scenario B with a S_{grm} of 30 (**a, c**) or 50% (**b, d**)

Fig. 14 Depth-specific resolution of changes in gas-phase saturation in the pore space (**a, b**) and relative hydraulic conductivity (**c, d**) for scenario B with assumed S_{grm}'s of 30% (**a, c**) or 50% (**b, d**) in S_5; markers in *black* indicate runtime when S_{grm} is reached; markers in *grey* indicate runtime when hydraulic conductivity is equivalent to the initial value at 10 °C

after S_{grm} has been reached will contribute to the excess gas volume (see "Effects on gas-phase saturation, heat conductivity and heat capacity in the zone of gas-phase accumulation by scenario calculations" section).

Possible sources for dissolved methane concentrations as assumed for scenario B are degradation processes of natural or pollutant OC (e.g. Appelo and Postma 2005), natural migration from deeper layers (e.g. Coldewey and
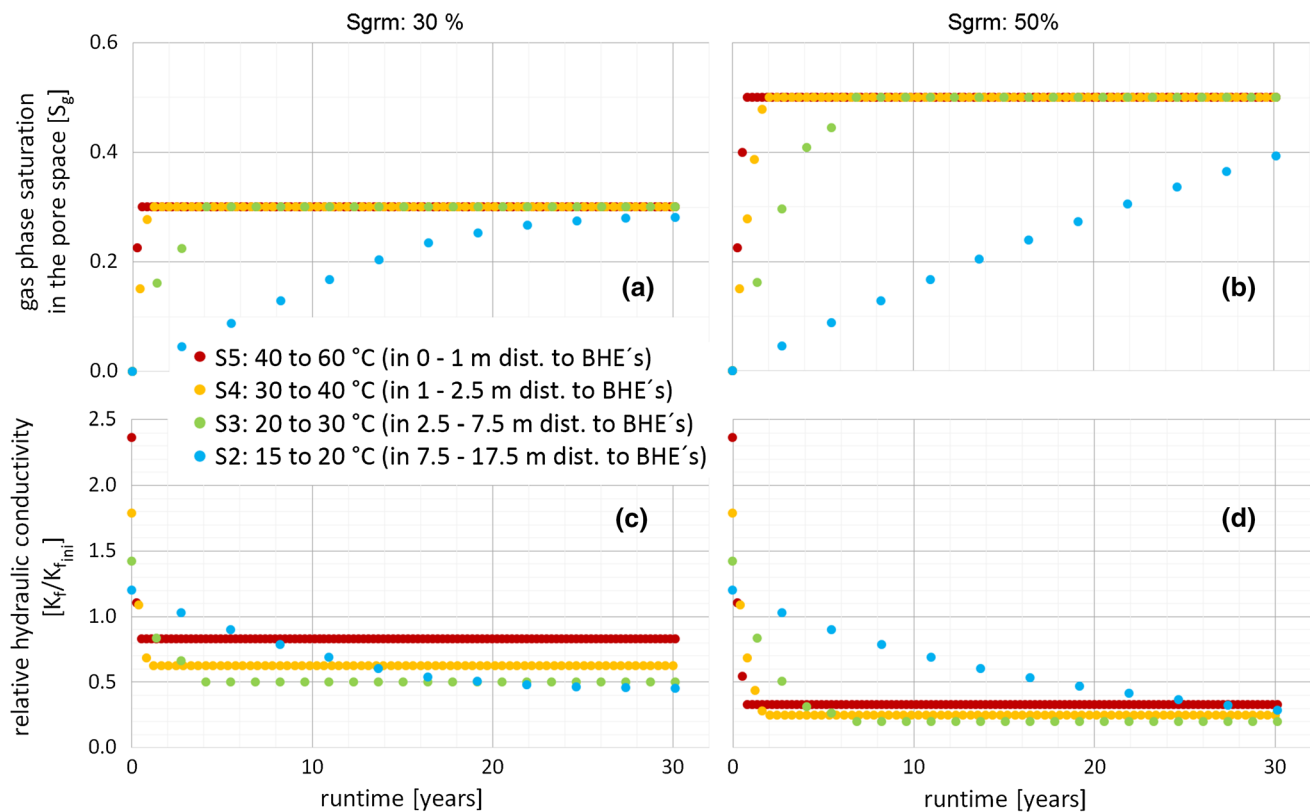
Fig. 15 Depth-averaged (over a 10-m-thick aquifer) development of gas-phase saturation in the pore space (**a**, **b**) and relative hydraulic conductivity (**c**, **d**) over 30 years of runtime as seasonal heat storage in case CO_2 is dissolved up to saturation in each depth (scenario C) with a S_{grm} of 30 (**a**, **c**) or 50% (**b**, **d**)

Melchers 2011; McIntosh et al. 2014) or leakages from production (or storage) wells (e.g. Van Stempvoort et al. 2005). The latter is not known to be a widespread problem in Germany but in case of increasing utilisation of the subsurface including gas storage in porous formations in the future (e.g. Pfeiffer and Bauer 2015), the possible impacts of leakages on the geochemistry of near-surface aquifers are already being investigated for ambient groundwater temperatures (Berta et al. 2015).

A S_{grm} of 30 (or 50) % in S_5 and S_4 is reached within the first (two) year(s) if CO_2 is dissolved up to saturation in addition to dissolved N_2 (scenario C; Fig. 15a/b). Basically, the same pattern is visible for the hydraulic conductivity, whereas the discrepancies between the different sections result from the deviation in the temperature effect on viscosity and density (Fig. 15c/d).

Dissolved CO_2 concentrations need to be about a magnitude higher to cause the formation of a separate gas phase compared to those of N_2 or CH_4. Such CO_2 concentrations probably only occur under special geochemical conditions as a natural upward migration of CO_2-bearing fluids (e.g. Battani et al. 2010; Fig. 10b). But under these special conditions, CO_2 exemplifies how fast gas-phase saturation can reach S_{grm} in S_3–S_5

(Fig. 15a/b). Gas being generated in these sections will migrate out of the zone of gas-phase formation for most of the 30-year runtime and contribute to the, accordingly huge, excess gas volume (see "Effects on gas-phase saturation, heat conductivity and heat capacity in the zone of gas-phase accumulation by scenario calculations" section).

Effects on gas-phase saturation, heat conductivity and heat capacity in the zone of gas-phase accumulation by scenario calculations

The gas-phase migration and therefore accumulation or degassing of a gas phase not trapped within the sediment start after 16 (>30), 14 (28) and 0.5 (0.8) years of runtime for S_{grm}'s of 30 (or 50) % in scenarios A, B and C, respectively (Fig. 16a). Under the corresponding total pressure conditions of 1.05, 2.05 and 3.05 atm for the top of the aquifer in scenarios A, B and C, the volume of the gas phase exceeding S_{grm} is limited to 1.4 and 5.7 m^3 in scenarios A and B, while in scenario C the gas-phase volume sums up to $\sim$900 and $\sim$650 m^3 for S_{grm}'s of 30 and 50% (Fig. 16a). The aquifers upper boundary morphology will control the migration pathway and potential
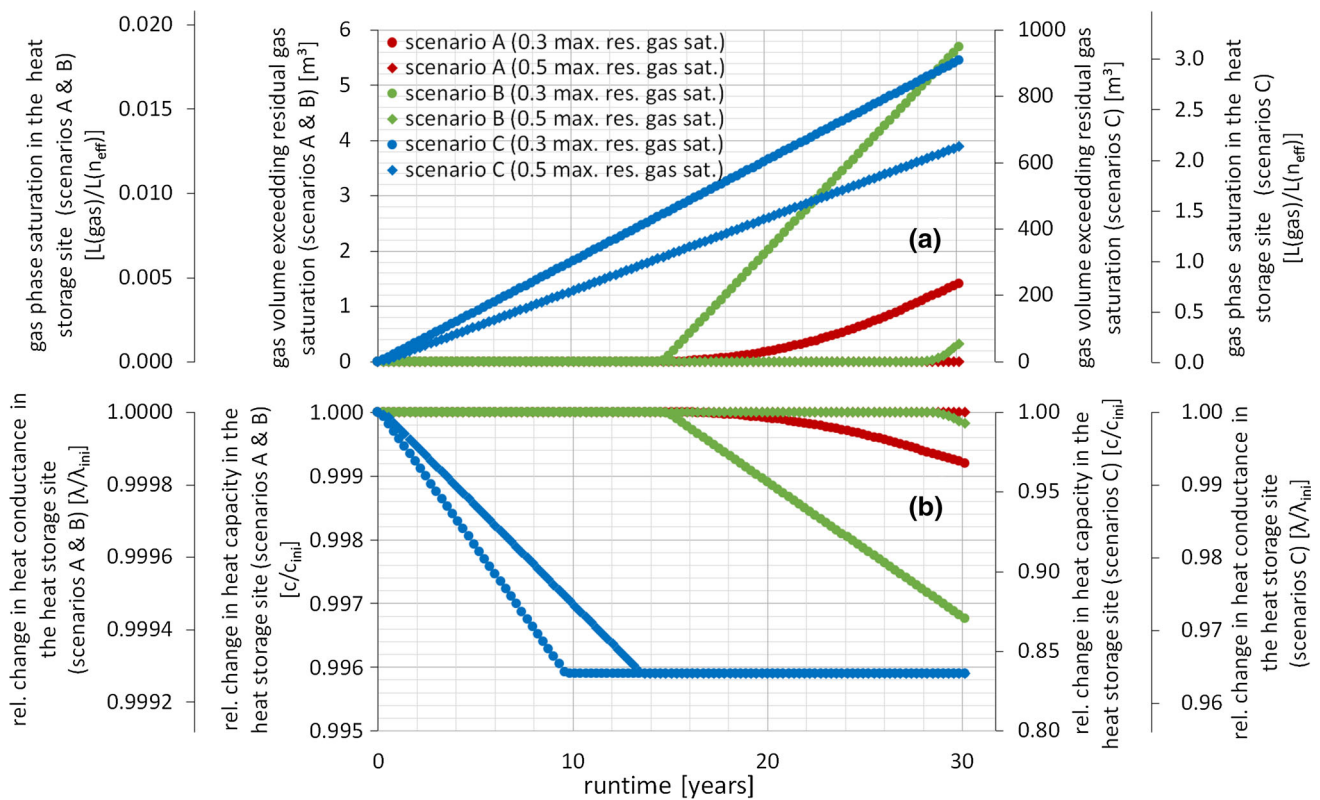
Fig. 16 Evolution of the excess gas-phase volume and the corresponding gas-phase saturation inside the heat storage site (**a**), evolution of relative changes in heat capacity and heat conductivity

(**b**) a gas-phase saturation within the heat storage site as displayed in (**a**) would cause, note that scenarios A and B are always displayed on the *left* y axis, while scenario C is displayed on the *right* y axis

accumulation in morphological traps of this excess gas phase.

During upward migration, the excess gas phase could be laterally diverted by the groundwater flow and thereby partly migrate into the heat storage site, which in the studied case extends 16 m in flow direction (2880 m^3 bulk volume). To estimate the maximum possible effects on the heat storage site itself, a case in which all excess gas phase migrates into the heat storage site was assumed. Thereby, average gas-phase saturation inside the heat storage site does not exceed 0.5 and 2% in scenarios A and B. In contrast, the excess gas volume generated in scenario C would exceed the accessible (effective) pore space (288 m^3) inside the heat storage site within 10 or 14 years of runtime for S_{grm}'s of 30 or 50% (Fig. 16a). These values result in a decrease in heat capacity by less than 0.1 and 0.4% in scenarios A and B at most. Heat capacity in scenario C decreases by a maximum of ~16% (Fig. 16b). The same pattern repeats in the evolution of heat conductivity as this is decreasing by less than 0.2 and 0.6 ‰ in scenarios A and B, and scenario C with 3% again shows a higher maximum decrease (Fig. 16b).

If only 0.85 mmol/L N_2 (equilibrium to a 1 atm N_2 gas phase) is present as a dissolved gas, effects of a gas-phase

formation on the gas-phase saturation and thus hydraulic conductivity are limited to the uppermost metres of the aquifer. Depending on the S_{grm} of an aquifer, the S_{grm} may be reached within the 30-year runtime or not. Even by assuming that all gas-phase formation after S_{grm} is reached is laterally shifted into the field of BHE, overall effects on porous media properties within the heat storage site as e.g. heat capacity and heat conductivity remain on the per ten thousand scale and are therefore most likely negligible.

The formation of a gas phase is not restricted to the upper metres of an aquifer but may go on also in deeper regions in case additional gases (as e.g. CH_4) are dissolved up to saturation due to an assumed source beside N_2. Nevertheless, in the short term, the effects on gas-phase saturation and hydraulic conductivity will still be limited, while in the long-term scale of 30 years, groundwater flow might be influenced considerably due to higher gas-phase saturations compared to the case when only N_2 is present as a dissolved gas. But impact on heat capacity and heat conductivity inside the heat storage site will still remain on the per mille scale.

Gas-phase formation in case CO_2 or H_2S is present in concentrations near solubility is on a higher scale: S_{grm} is reached within a year in the direct vicinity of the BHE and

is also reached within a few years in the farther away sections. In case further generated gas phase migrates out of the zone of gas-phase formation, gas-phase formation will go on over the whole 30-year runtime resulting in the build-up of a large excess gas volume, probably either spreading widely at the top of the aquifer or accumulating in morphological traps. Also the impact on heat capacity and heat conductivity inside the heat storage site might reach values that considerably affect sites efficiency.

Discussion

Column experiments as conducted within this study are a direct but time- and resource-consuming method to determine gas-phase formation ratios. Thermodynamic calculations reproduced the high experimental gas-phase formation ratios at 70 °C with <2.5% deviation. Thus, thermodynamic calculations are a feasible approach to assessing, at least high, gas-phase formation ratios and enable to state necessity of additional experimental investigations.

Groundwater in equilibrium with atmospheric partial pressures or with an increased CO_2 partial pressure of soil air (Matthes 1990) causes a gas-phase formation only down to water-saturated depths of 12 or 13 m, respectively, in case of heating to 70 °C. A gas-phase formation at greater depths is only initiated if initial dissolved gas concentrations are increased, which might either be caused by natural upward migration of CH_4 or CO_2 from deeper layers or by degradation of natural or pollutant OC. However, degradation of OC probably will not play a major role for dissolved gas concentrations in the highly permeable, poor in OC, northern German aquifers used as background for calculations within this study unless there is e.g. a source zone of organic pollutants (e.g. Feisthauer et al. 2012). Considerable contribution of OC degradation to dissolved gas concentrations occurs in limnic sediments with CH_4 concentrations going up to 1 mmol/L (e.g. Schulz and Conrad 1995; Juutinen et al. 2009) or with even higher CH_4 concentrations in marine sediments (e.g. Reeburgh 2007). Thus, especially at increased temperatures (Bonte et al. 2013a; Jesußek et al. 2013) and in OC-rich, cohesive sediments, increased dissolved gas concentrations due to degradation processes can be expected. Though, in contrast to limnic or marine sediments beside CH_4 also dissolved N_2 concentrations can be increased in case of high nitrate concentrations caused by agricultural land use (e.g. Wendland et al. 1998; Puckett and Cowdery 2002; Visser et al. 2009).

Appearing gas-phase saturations and subsequent decreases in hydraulic conductivity in the heat storage setting used here vary from very restricted to more substantial in the three scenario calculations. For a frequent setting like scenario A, gas-phase saturation only slowly increases with time, which results in comparable small effects on aquifer hydraulics in the first years of runtime. But as the gas phase accumulates over time, a S_{grm} of 30% in the most affected S_5 is reached during 30 years in the upper 7 m. Independently from the S_{grm} or the applied scenario, the temperature-induced focused flow due to viscosity and density effects is at least counterbalanced in the direct vicinity of the BHEs (S_5). In consequence, also a gas-phase formation appearing marginal in the first year(s) of operation should be quantified to estimate long-term evolution. Back dissolution of former generated gas phase could occur in periods without heating if the inflowing water is not saturated with dissolved gases. Therefore, gas-phase accumulation would slow down in scenario A, but would not change in scenarios B and C due to gas-saturated conditions.

Gas-phase accumulation over time is considerably controlled by the groundwater flow velocity as this linearly corresponds to pore water replacement in the heated zone of an aquifer. Van Loon (1991) states a groundwater flow velocity <0.03 or <0.11 m/d as suitable for small (25 m^3/h) or large ATES projects (500 m^3/h), respectively. Nevertheless, groundwater flow velocities one or two magnitudes higher may occur in aquifers mainly consisting of middle- or coarse-grained sands (e.g. Pannike et al. 2006). In addition to the correspondingly faster gas-phase accumulation due to the increased groundwater flow velocity, the temperature profile upstream of the heat storage site would become steeper due to a shift in heat propagation from more diffusive controlled to more advective controlled. This would result in an even more focused gas-phase formation, accumulation and subsequent migration directly upstream the heat storage site.

Another crucial factor for the spatiotemporal distribution of a forming gas phase is the S_{grm} of a sediment as this value controls whether a smaller or larger amount of gas phase stays within the zone of gas-phase formation or starts to migrate. Values for S_{grm}'s reported in the literature show a wide range from 14 to 55% (Fry et al. 1997) with other studies lying in between [e.g. Istok et al. (2007) (20%) or Ye et al. (2009) (40–50%)]. Krol et al. (2011) attributed the difference in S_{grm} of different sediments or sands to pore and grain size distribution. The column experiments done within this study showed S_{grm} of ~ 25, ~ 60 and $\sim 70\%$ in the zone of gas-phase formation in the columns heated to 25, 40 and 70 °C indicating an influence of the temperature-dependent fluid- and gas-phase properties on the S_{grm}. In settings where due to the interplay between temperature, pressure and dissolved gas concentrations a considerable gas-phase formation can be expected, S_{grm} should be site-specifically estimated, as the

S_{grm} controls the maximum decrease in hydraulic conductivity. Accumulation of a gas phase does not only lead to subsequent changes in hydraulic conductivity but will also effect porous media properties as heat conductivity, heat capacity and geotechnical behaviour. Overall effects on heat conductivity and heat capacity of a heat storage site will remain rather low in this study's aquifer settings in case no dissolved gas concentrations near saturation of CO_2 (or H_2S), as used in scenario C, are present. This might be different in OC-rich, cohesive sediments as gas-phase formation can be enhanced by degradation processes. Furthermore, low permeability can limit gas-phase migration causing an accumulation of gas phase exceeding S_{grm} within the zone of gas-phase formation and thus intensify impact on heat conductivity, heat capacity and geotechnical behaviour. Especially for near-surface heat storage applications within urban areas, the question how subsurface geotechnical behaviour is affected by gas-phase saturations up to 70% has to be addressed in the future.

However, the formation of a gas phase cannot be seen particularly positive or negative in general in terms of efficiency. In a heat storage site where heat is injected and extracted by a field of borehole heat exchangers (BTES), any decrease in groundwater flow, due to wide-ranging flow deflection caused by the formation of a gas phase directly upstream of a heat storage site, will reduce the advective loss of heat to the surrounding aquifer and thus can increase the sites efficiency. On the contrary, in any heat storage site where water is injected and extracted to store heat (ATES), a gas phase would lead to a wider distribution of the injected water and thus probably lower the sites efficiency by reducing recoverability of the heated water. By aiming at disposal of heat from e.g. industrial processes or building climatisation, a wide-ranging flow deflection would lower heat dissipation and thus efficiency.

Degassing of O_2 or CO_2 can facilitate the development of reducing conditions or increase carbonate (over)saturation. In contaminated aquifers also pollutants can partition into a gas phase and might be transported into former uncontaminated zones. Collapsing of a gas phase by redissolution in case of migration into cooler areas of the aquifer could induce the reverse impacts on groundwater properties and thus in case of pollutants enlarge the contaminated area (Krol et al. 2011). Further, gas-phase formation due to heat storage in a contaminated aquifer (e.g. Popp et al. 2015) can lower mass discharge or supply of electron acceptors for microbial degradation processes by deflection of the groundwater flow.

Due to the lack of efficient high-spatial-resolution monitoring methods in field, the geophysical approach of ER measurements was tested here. Since increasing temperatures and gas-phase accumulation affect the electrical behaviour of sediments antithetically, time-lapse ER measurements should enable to derive these effects differentiated from baseline measurements. In this study, the successful application monitoring of the temperature variations in the eight measurement segments based on the arrangement of the cannulas was demonstrated. Thus, the resistivity changes could be monitored in the vertical axes and ensure a spatial resolution to localise possible differing processes such as gas-phase formation and outgassing pathways. The results showed the strong and immediate onset of the effect of the different temperatures for each column after the baseline measurements. The resistivity changes correlated with empirical equations for the temperature dependence based on established literature. In contrast, the influence of the temperature-induced chemical reactions can be negligible for the ER variations. Further, anomalies detected in the lowest measurement segments of each of the different heated columns in the experimental runtime could not be explained by the increased temperature since the electrical resistivities indeed increased. These increased resistivity values can be explained by decreased water saturation. This suggestion corresponds to the studies of Istok et al. (2007) and Ye et al. (2009) as the gas phase is formed in the lowest part of the columns where the cooler infiltrated water is mostly affected by the heating process. However, since no resistivity anomalies could have been observed for the central measurement segments, the monitoring does not show any outgassing phases of the collected gas in the gas trapping bottles. Further, based on the arrangement of the cannulas, the upper 15 cm of the columns could not have been monitored, and thus, the measurements do not observe possible gas accumulations in the upper segments of the heated columns. Therefore, further work on laboratory scale should include different electrode arrangements and configurations for an optimised spatial resolution and the possible gas-phase accumulations at the top of the columns. Since the electrode layout in the presented study was entailed due to the arrangement of the cannulas, more electrodes should be used at the sidewalls and circular around the columns, as well as at the bases of the columns in order to have a complete 3D monitoring as shown by Comina et al. (2010).

To summarise, the interplay between dissolved gas content, surrounding pressure and applied temperature increase determines whether TES causes gas-phase formation and if so also its extent. Generally spoken, if the groundwater's gas content and the increase in temperature are low while the surrounding pressure is high, a gas-phase formation is unlikely. In contrast, a gas-phase formation is likely in case the groundwater's gas content and the increase in temperature is high while the surrounding pressure is low. In case of gas-phase formation,

groundwater flow velocity and temperature gradient in the aquifer control the gas-phase spatiotemporal accumulation and distribution. Since all these boundary conditions can site-specifically vary to a considerable extent and the type (ATES/BTES) and dimensioning of an application additionally plays a vital role on the gas-phase formation potential, the possibility for a gas-phase formation and its effects should generally be examined during planning of TES applications.

References

Alikhani J, Deinhart AL, Visser A, Bibby RK, Purtschert R, Moran JE, Massoudieh A, Esser BK (2016) Nitrate vulnerability projections from Bayesian inference of multiple groundwater age tracers. J Hydrol. doi:10.1016/j.jhydrol.2016.04.028

Amos RT, Mayer KU (2006) Investigating the role of gas bubble formation and entrapment in contaminated aquifers: reactive transport modelling. J Contam Hydrol 87:123–154. doi:10.1016/j.jconhyd.2006.04.008

Amos RT, Mayer KU, Bekins BA, Delin GN, Williams RL (2005) Use of dissolved and vapor-phase gases to investigate methanogenic degradation of petroleum hydrocarbon contamination in the subsurface. Water Resour Res 41:1–15. doi:10.1029/2004WR003433

Andrews WJ, Stark JR, Fong AL, Fallon JD (2005) Water-quality assessment of part of the upper Mississippi River Basin, Minnesota and Wisconsin—Ground-water quality along a flow system in the Twin Cities Metropolitan Area, Minnesota, 1997–1998. Scientific Investigations Report 2005–5120

Appelo CAJ, Postma D (2005) Geochemistry, groundwater and pollution, 2nd edn. A.A. Balkema Publishers, Leiden

Archie GE (1942) The electrical resistivity log as an aid in determining some reservoir characteristics. J Pet Technol 5:54–62

Arning E, Kölling M, Schulz HD, Panteleit B, Reichling J (2006) Einfluss oberflächennaher Wärmegewinnung auf geochemische Prozesse im Grundwasserleiter. Grundwasser 11:27–39. doi:10.1007/s00767-006-0116-0

Battani A, Deville E, Faure JL, Jeandel E, Noirez S, Tocqué E, Benoît Y, Schmitz J, Parlouar D, Sarda P, Gal F, le Pierres K, Brach M, Braibant G, Beny C, Pokryszka Z, Charmoille A, Bentivegna G, Pironon J, de Donato P, Garnier C, Cailteau C, Barrès O, Radilla G, Bauer A (2010) Geochemical study of natural CO_2 emissions in the French massif central: how to predict origin, processes and evolution of CO_2 leakage. Oil Gas Sci Technol 65:615–633. doi:10.2516/ogst/2009052

Bauer S, Pfeiffer T, Boockmeyer A, Dahmke A, Beyer C (2015) Quantifying induced effects of subsurface renewable energy storage. Energy Proc 76:633–641. doi:10.1016/j.egypro.2015.07.885

Beaubien SE, Ciotoli G, Lombardi S (2003) Carbon dioxide and radon gas hazard in the Alban Hills area (central Italy). J Volcanol Geotherm Res 123:63–80. doi:10.1016/S0377-0273(03)00028-3

Bergmann P, Schmidt-Hattenberger C, Kiessling D, Rücker C, Labitzke T, Henninges J, Baumann G, Schütt H (2012) Surface-downhole electrical resistivity tomography applied to monitoring of CO_2 storage at Ketzin, Germany. Geophysics 77:B253–B267. doi:10.1190/geo2011-0515.1

Berta M, Becker A, Dethlefsen F, Ebert M, Koch S, Dahmke A (2015) Experiments showed no reactions coupled to methane leaked into shallow aquifers. First Break 33:93–95

Blicher-Mathiesen G, McCarty GW, Nielsen LP (1998) Denitrification and degassing in groundwater estimated from dissolved dinitrogen and argon. J Hydrol 208:16–24. doi:10.1016/S0022-1694(98)00142-5

BMWi (2015) Erneuerbare Energien im Jahr 2014. Bundesministerium für Wirtschaft und Energie, Berlin

Bockelmann F, Fisch MN, Kühl L, Petruszek T, Nüßle F, Sanner B (2012) Optimization of ground coupled heating and cooling supply systems in office buildings—reversible heat pump and free cooling. In: Proceedings of the 12th international conference on energy storage, Innostock, Spain

Bonte M (2013) Impacts of shallow geothermal energy on groundwater quality—a hydrochemical and geomicrobial study of the effects of ground source heat pumps and aquifer thermal energy storage. VU University Amsterdam, Amsterdam

Bonte M, Stuyfzand PJ, Hulsmann A, Van Beelen P (2011) Underground thermal energy storage: environmental risks and policy developments in the Netherlands and European Union. Ecol Soc 16:22

Bonte M, Röling WFM, Zaura E, Van Der Wielen PWJJ, Stuyfzand PJ, Van Breukelen BM (2013a) Impacts of shallow geothermal energy production on redox processes and microbial communities. Environ Sci Technol 47:14476–14484. doi:10.1021/es4030244

Bonte M, van Breukelen BM, Stuyfzand PJ (2013b) Temperature-induced impacts on groundwater quality and arsenic mobility in anoxic aquifer sediments used for both drinking water and shallow geothermal energy production. Water Res 47:5088–5100. doi:10.1016/j.watres.2013.05.049

Bridger DW, Allen DM (2005) Designing aquifer thermal energy storage systems. ASHRAE J 47:32–37

Brons HJ, Griffioen J, Appelo CAJ, Zehnder AJB (1991) (Bio)geochemical reactions in aquifer material from a thermal energy storage site. Water Res 25:729–736. doi:10.1016/0043-1354(91)90048-U

Brunet P, Clément R, Bouvier C (2010) Monitoring soil water content and deficit using Electrical Resistivity Tomography (ERT)—a case study in the Cevennes area, France. J Hydrol 380:146–153

Carrigan CR, Yang X, LaBrecque DJ, Larsen D, Freeman D, Ramirez AL, Daily W, Aines R, Newmark R, Friedmann J, Hovorka S (2013) Electrical resistance tomographic monitoring of CO_2 movement in deep geologic reservoirs. Int J Greenh Gas Control 18:401–408. doi:10.1016/j.ijggc.2013.04.016

Chiodini G, Frondini F (2001) Carbon dioxide degassing from the Albani Hills volcanic region, Central Italy. Chem Geol 177:67–83

Coldewey WG, Melchers C (2011) Gas im Münsterland—Gefahren und Nutzung. In: 62. Deutsche Brunnenbauertage und BAW-Baugrundkolloquium "Baugrundaufschlüsse: Planung, Ausschreibung, Durchführung, Überwachung und Interpretation" 13–15. April 2011 im Bau-ABC Rostrup/Bad Zwischenahn. Münster, p 2

Comina C, Cosentini RM, Della Vecchia G, Foti S, Musso G (2010) Hydro-chemo-mechanical processes in soil samples: monitoring through electrical resistivity tomography. EPJ Web Conf 6:22012. doi:10.1051/epjconf/20100622012

Corwin DL, Lesch AM (2005) Apparent soil electrical conductivity measurements in agriculture. Comput Electron Agric 46:11–43

Dachnov VN (1962) Interpretazija resultatov geofiziceskich issledovanij skvazin, 2nd edn. Izdat. Gostoptechizdat, Moscow

Daily W, Ramirez A, LaBreque D, Nitao J (1992) Electrical resistivity tomography of vadose water movement. Water Resour Res 28:1429–1442

Debenedetti PG (1996) Metastable liquids: concepts and principles. Princeton University Press, Princeton

Dietrich P (1999) Konzeption und Auswertung gleichstromgeoelektrischer Tracerversuche unter Verwendung von Sensitivitätskoeffizienten. University of Tübingen, Tübingen

Feast NA, Hiscock KM, Dennis PF, Andrews JN (1998) Nitrogen isotope hydrochemistry and denitrification within the Chalk aquifer system of north Norfolk, UK. J Hydrol 211:233–252

Feisthauer S, Seidel M, Bombach P, Traube S, Knöller K, Wange M, Fachmann S, Richnow HH (2012) Characterization of the relationship between microbial degradation processes at a hydrocarbon contaminated site using isotopic methods. J Contam Hydrol 133:17–29. doi:10.1016/j.jconhyd.2012.03.001

Ferguson G (2009) Unfinished business in geothermal energy. Ground Water 47:167. doi:10.1111/j.1745-6584.2008.00528.x

Friedman SP (2005) Soil properties influencing apparent electrical conductivity: a review. Comput Electron Agric 46:45–70. doi:10.1016/j.compag.2004.11.001

Friedman SP, Seaton NA (1998) Critical path analysis of the relationship between permeability and electrical conductivity of three-dimensional pore networks. Water Resour Res 34:1703–1710

Fry VA, Selker JS, Gorelick SM (1997) Experimental investigations for trapping oxygen gas in saturated porous media for in situ bioremediation. Water Resour Res 33:2687–2696. doi:10.1029/97WR02428

Giordano N, Firmbach L, Comina C, Dietrich P, Mandrone G, Vienken T (2013) Laboratory scale electrical resistivity measurements to monitor the heat propagation within porous media for low enthalpy geothermal applications. In: Proceedings of the 32nd conference of the national group of solid earth geophysics—GNGTS, Trieste, Italia, 2013

Giordano N, Comina C, Mandrone G (2015) The first Italian experience of ground thermal energy storage: an integrated approach for design and monitoring, from laboratory to field scale. In: Proceedings of the world geothermal congress, Melbourne, Australia, 2015

Grellier S, Bouyé JM, Guérin R, Robain H, Skhiri N (2005) Electrical Resistivity Tomography (ERT) applied to moisture measurements in bioreactor: principles, in situ measurements and results. In: Proceedings of the international workshop of "Hydro-Physico-Mechanics of Landfills" LIRIGM, Grenoble, France, 2005

Griffioen J, Appelo CAJ (1993) Nature and extent of carbonate precipitation during aquifer thermal energy storage. Appl Geochem 8:161–176. doi:10.1016/0883-2927(93)90032-C

Gunn DA, Chambers JE, Uhlemann S, Wilkinson PB, Meldrum PI, Dijkstra TA, Haslam E, Kirkham M, Wragg J, Holyoake S, Hughes PN, Hen-Jones R, Glendinning S (2014) Moisture monitoring in clay embankments using electrical resistivity tomography. Constr Build Mater 92:82–94

Hähnlein S, Bayer P, Blum P (2010) International legal status of the use of shallow geothermal energy. Renew Sustain Energy Rev 14:2611–2625. doi:10.1016/j.rser.2010.07.069

Hem JD (1985) Study and interpretation of the chemical characteristics of natural water. Department of the Interior, US Geological Survey, Reston, VA

Hermans T, Vandenbohede A, Lebbe L, Nguyen F (2012) A shallow geothermal experiment in a sandy aquifer monitored using electric resistivity tomography. Geophysics 77:11–21

Hermans T, Wildemeersch S, Jamin P, Orban P, Broyère S, Dassargues A, Nguyen F (2015) Quantitative temperature monitoring of heat tracing experiment using cross-borehole ERT. Geothermics 53:14–26

Hoffmann R, Dietrich P (2004) Geoelektrische Messungen zur Bestimmung von Grundwasserfließrichtungen und -geschwindigkeiten. Grundwasser 3:194–203

Holm TR, Eisenreich SJ, Rosenberg HL, Holm NP (1987) Groundwater geochemistry of short-term aquifer thermal energy storage test cycles. Water Resour Res 23:1005–1019

IEA (2015) Energy technology perspectives 2015. International Energy Agency, Paris

Istok JD, Park MM, Peacock AD, Oostrom M, Wietsma TW (2007) An experimental investigation of nitrogen gas produced during denitrification. Ground Water 45:461–467. doi:10.1111/j.1745-6584.2007.00319.x

Jenne EA, Andersson O, Willemsen A (1992) Well, hydrology, and geochemistry problems encountered in ATES systems and their solutions. In: Proceedings of the intersociety energy conversion engineering conference

Jesußek A, Grandel S, Dahmke A (2013) Impacts of subsurface heat storage on aquifer hydrogeochemistry. Environ Earth Sci 69:1999–2012. doi:10.1007/s12665-012-2037-9

Juutinen S, Rantakari M, Kortelainen P, Huttunen JT, Larmola T, Alm J, Silvola J, Martikainen PJ (2009) Methane dynamics in different boreal lake types. Biogeosciences 6:209–223. doi:10.5194/bg-6-209-2009

Keller GV, Frischknecht FC (1966) Electrical methods in geophysical prospecting. Pergamon Press, Oxford

Knödel K, Krummel H, Lange G (2005) Handbuch zur Erkundung des Untergrundes von Deponien und Altlasten—Band 3: Geophysik. Springer, Berlin

Krol MM, Mumford KG, Johnson RL, Sleep BE (2011) Modeling discrete gas bubble formation and mobilization during subsurface heating of contaminated zones. Adv Water Resour 34:537–549. doi:10.1016/j.advwatres.2011.01.010

Lide DR (2005) CRC handbook of chemistry and physics, Internet version. CRC Press, Boca Raton

Llera FJ, Sato M, Nakatsuka K, Yokoyama H (1990) Temperature dependence of the electrical resistivity of water-saturated rocks. Geophysics 55:576–585

Ma R, McBratney A, Whelan B, Minasny B, Short M (2011) Comparing temperature correction models for soil electrical conductivity measurement. Precis Agric 12:55–66

Matthes G (1990) Die Beschaffenheit des Grundwassers, 2nd edn. Gebrüder Bornträger, Berlin

McCleskey RB, Nordstrom DK, Ryan JD (2011) Electrical conductivity method for natural waters. Appl Geochem 26:227–229

McIntosh JC, Grasby SE, Hamilton SM, Osborn SG (2014) Origin, distribution and hydrogeochemical controls on methane occurrences in shallow aquifers, southwestern Ontario, Canada. Appl Geochem 50:37–52. doi:10.1016/j.apgeochem.2014.08.001

Mualem Y, Friedman SP (1991) Theoretical prediction of electrical conductivity in saturated and unsaturated soil. Water Resour Res 27:2771–2777

Palmer CD, Cherry JA (1984) Geochemical reactions associated with low-temperature thermal energy storage in aquifers. Can Geotech J 21:475–488. doi:10.1139/t84-051

Pannike S, Kölling M, Schulz HD, Panteleit B, Reichling J, Scheps V (2006) Auswirkung hydrogeologischer Kenngrößen auf die Kältefahnen von Erdwärmesondenanlagen in Lockersedimenten. Grundwasser 11:6–18. doi:10.1007/s00767-006-0114-2

Parkhurst DL, Appelo CAJ (2013) Description of input and examples for PHREEQC version 3—a computer program for speciation, batch-reaction, one-dimensional transport, and inverse geochemical calculations. In: U.S. geological survey techniques and methods, book 6. p 497

Pfeiffer WT, Bauer S (2015) Subsurface porous media hydrogen storage—scenario development and simulation. Energy Proc 76:565–572. doi:10.1016/j.egypro.2015.07.872

Popp S, Beyer C, Dahmke A, Bauer S (2015) Model development and numerical simulation of a seasonal heat storage in a contaminated shallow aquifer. Energy Procedia 76:361–370. doi:10.1016/j.egypro.2015.07.842

Possemiers M, Huysmans M, Batelaan O (2014) Influence of Aquifer Thermal Energy Storage on groundwater quality: a review illustrated by seven case studies from Belgium. J Hydrol Reg Stud 2:20–34. doi:10.1016/j.ejrh.2014.08.001

Puckett LJ, Cowdery TK (2002) Transport and fate of nitrate in a glacial outwash aquifer in relation to ground water age, land use practices, and redox processes. J Environ Qual 31:782–796

Reeburgh W (2007) Oceanic methane biogeochemistry. Am Chem Soc 107:486–513. doi:10.1021/cr050362v

Rhoades JD, Chanduvi F, Lesch S (1999) Soil salinity assessment: methods and interpretation of electrical conductivity measurements. Food and Agriculture Organization of the United Nations, Rome

Richards LA (1954) Diagnoses and improvement of saline and alkaline soils. U.S. Department of Agriculture, Washington, DC

Robinson DA, Friedman SP (2003) A method for measuring the solid particle permittivity or electrical conductivity of rocks, sediments, and granular materials. J Geophys Res 108:2076. doi:10.1029/2001JB000691

Saito T, Hamamoto S, Ueki T, Ohkubo S, Moldrup P, Kawamoto K, Komatsu T (2016) Temperature change affected groundwater quality in a confined marine aquifer during long-term heating and cooling. Water Res 94:120–127. doi:10.1016/j.watres.2016.01.043

Sanchez de Lozada D, Vandevivere P, Baveye P, Zinder S (1994) Decrease of the hydraulic conductivity of sand columns by Methanosarcina barkeri. World J Microbiol Biotechnol 10:325–333. doi:10.1007/BF00414873

Schmidt T, Müller-Steinhagen H (2005) Erdsonden- und Aquifer-Wärmespeicher in Deutschland. In: OTTI, Profiforum Oberflächennahe Geothermie. Regenstauf, pp 1–12

Schroth MH, Istok JD, Ahearn SJ, Selker JS (1996) Characterization of miller-similar silica sands for laboratory hydrologic studies. Soil Sci Soc Am J 60:1331. doi:10.2136/sssaj1996.03615995006000050007x

Schulz S, Conrad R (1995) Effect of algal deposition on acetate and methane concentrations in the profundal sediment of a deep lake (Lake Constance). FEMS Microbiol Ecol 16:251–260

Shipton ZK, Evans JP, Dockrill B, Heath J, Williams A, Kirchner D, Kolesar PT (2005) Natural leaking CO_2- charged systems as analogs for failed geologic storage reservoirs. In: Thomas DC, Benson SM (eds) Carbon dioxyde CO_2 capture for storage in deep geologic formations. Elsevier, Amsterdam, pp 699–712

Tesoriero AJ, Liebscher H, Cox SE (2000) Mechanism and rate of denitrification in an agricultural watershed: electron and mass balance along groundwater flow paths. Water Resour Res 36:1545–1559

van Genuchten MT (1980) A closed-form equation for predicting the hydraulic conductivity of unsaturated soils. Soil Sci Soc Am J 44:892–898. doi:10.2136/sssaj1980.03615995004400050002x

van Loon LJM (1991) Relevant characteristics for open (ATES) storage. In: Chant VG (ed) IEA ECES annex7 - Proceedings workshop on generic configuration of seasonal cold storage applications, Utrecht, Sept 18–19,1991. International Energy Agency, Paris

Van Stempvoort D, Maathuis H, Jaworski E, Mayer B, Rich K (2005) Oxidation of fugitive methane in ground water linked to bacterial sulfate reduction. Groundwater 43:187–199

Visser A, Broers HP, Bierkens MFP (2007) Dating degassed groundwater with 3H/3He. Water Resour. Res. doi:10.1029/2006WR005847

Visser A, Schaap JD, Peter HP, Bierkens MFP (2009) Degassing of 3H/3He, CFCs and SF6 by denitrification: measurements and two-phase transport simulations. J Contam Hydrol 103:206–218. doi:10.1016/j.jconhyd.2008.10.013

Visser A, Singleton M, Madrid V, Esser B (2014) Summary and preliminary interpretation of tritium and dissolved noble gas data from site 300. Lawrence Livermore National Laboratory LLNLTR- 649041

Vogel JC, Talma AS, Heaton THE (1981) Gaseous nitrogen as evidence for denitrification in groundwater. J Hydrol 50:191–200

Wendland F, Bach M, Kunkel R (1998) In: Finke PA, Bouma J, Hoosbeek MR (eds) Soil and water quality at different scales: proceedings of the workshop "Soil and Water Quality at Different Scales'' held 7–9 August 1996, Wageningen, The Netherlands. Springer, Dordrecht, pp 167–179

Willemsen A, Appelo CAJ (1985) Chemical reactions during heat storage in shallow aquifers in the netherlands: laboratory experiments and Geochemical Modelling. In: Hydrogeology in the service of man, mémoires of the 18th congress of the international association of hydrogcologists. Cambridge, pp 68–78

Wilson GB, Andrews JN, Bath AH (1990) Dissolved gas evidence for denitrification in the Lincolnshire Limestone aquifer, eastern England. J Hydrol 113:51–60

Yang X, Lassen RN, Jensen KH, Looms MC (2015) Monitoring CO_2 migration in a shallow sand aquifer using 3D crosshole electrical resistivity tomography. Int J Greenh Gas Control 42:534–544. doi:10.1016/j.ijggc.2015.09.005

Ye S, Sleep BE, Chien C (2009) The impact of methanogenesis on flow and transport in coarse sand. J Contam Hydrol 103:48–57. doi:10.1016/j.jconhyd.2008.09.004